



# Evaluation Procedures for the Potential Harmonic Coefficients of a Generally Shaped Polyhedron

Georgia Gavriilidou<sup>1</sup> · Dimitrios Tsoulis<sup>1</sup>

Received: 27 January 2023 / Accepted: 12 July 2023  
© The Author(s), under exclusive licence to Springer Nature B.V. 2023

## Abstract

Two computational strategies for the evaluation of the spherical harmonic coefficients of the gravitational potential due to a generally shaped homogeneous polyhedral source are examined in detail. The techniques are implemented numerically for the known asteroid shape models of Eros and Didymos. The aim of the investigation is to quantify specific numerical aspects of the two algorithms, such as the accuracy of the techniques compared to a closed analytical solution for varying distance between source and computation point, the band-limited spectral analysis of the obtained spherical harmonic models and the convergence behavior of the corresponding series expansion in the vicinity of the characteristic Brillouin sphere. From a computational point of view, the line integral approach demands approximately three times the CPU time of Werner's method. The two sets of spherical harmonic coefficients are 100% correlated up to degree 45 for Eros and up to degree 49 for Didymos. Approaching degree 100, the correlation by degree decreases by 0.0004% for Eros and by 0.004% for Didymos, the corresponding values for the correlation by order being 0.0002% and 0.304%. Inside the Brillouin sphere and approaching its boundary, the numerical agreement of the gravitational potential between the line integral method and the analytical solution is at the  $1\text{E}-4$  level, while with Werner's approach at the  $1\text{E}-7$  level. At a distance of 33.5 km outside the Brillouin sphere for Eros and 2.2 km for Didymos, both methods are identical, reaching an agreement level with the analytical solution of  $1\text{E}-11$  level for Eros and  $1\text{E}-14$  for Didymos. In terms of spherical harmonic representation, the series defined by the line integral approach converges faster to the analytical value for the gravitational potential by 4 degrees.

**Keywords** Gravitational potential · General polyhedron · Spherical harmonics · Numerical integration

---

✉ Georgia Gavriilidou  
[georgiaga@topo.auth.gr](mailto:georgiaga@topo.auth.gr)

Dimitrios Tsoulis  
[tsoulis@auth.gr](mailto:tsoulis@auth.gr)  
<http://users.auth.gr/tsoulis>

<sup>1</sup> Department of Geodesy and Surveying, Aristotle University of Thessaloniki, GR 54 124 Thessaloniki, Greece

## Article Highlights

- The line integral approach and Werner's method for the computation of the potential harmonic coefficients of a polyhedral source are evaluated numerically
- The comparison of the two algorithms with the closed analytical solution for the polyhedral gravity signal shows an agreement of both methods in the range  $[1\text{E-}4\text{ }1\text{E-}11]$
- An implementation to the real shape data of asteroids Eros and Didymos reveals that the line integral approach converges faster to the analytical solution by 4 harmonic degrees

## 1 Introduction

The evaluation of the gravitational potential function and its spatial derivatives induced by known mass distributions is a central topic in gravity field modeling and interpretation. When considering real or idealized three-dimensional mass distributions the intended task is the numerical computation of Newton's triple integral defining the desired functional. The evaluation in question can be performed either analytically or numerically. Analytical methods provide closed exact solutions for the requested functionals, while numerical techniques approximate the sought quantities either by means of numerical integration or by expressing the functionals in terms of a harmonic series expansion.

Both solutions depend on the geometry adopted to represent the mass distribution. For the analytical approach, a typical shape selection, widely used in terrain modeling studies, is the right rectangular prism, whose potential and spatial derivatives can be evaluated analytically by a direct stepwise solution of the corresponding triple integrals in Cartesian coordinates (Nagy et al. 2000; Tsoulis 2000). A more versatile tool, able to represent arbitrary mass distributions in more detail, is the generally shaped polyhedron. The gravity field defined by a polyhedral source can also be evaluated analytically. The different proposed methodologies roughly adopt the common principle of subsequently applying the Gauss, Stokes or Green theorems, which transform the triple integrals into two- and one-dimensional integrals, leading eventually to analytical solutions defined across polyhedral edges and faces (Werner 1994; Singh and Guptasarma 2001; Saraswati et al. 2019; D'Urso 2014a, b; Petrović 1996; Tsoulis and Petrović 2001; Tsoulis 2012; Tsoulis and Gavrilidou 2021).

In the context of numerical methods, some of the first proposed algorithms for the computation of potential harmonic coefficients induced by a given mass distribution are those of Colombo (1981), Cunningham (1970) and Gottlieb (1993). The solution of Chao and Rubincam (1989) replaces the radius vector describing the mass distribution's shape with a series of infinite terms while Balmino (1994) solves the spherical harmonic expansion of the gravitational potential analytically. Werner (1997) divides the solid body into tetrahedra and provides a recursive algorithm for the computation of the spherical harmonic coefficients using the integration technique of Lien and Kajiya (1984), while Chen et al. (2019) also apply a tetrahedral division of the given mass distribution, using a variable density.

Jamet and Thomas (2004) proposed a linear algorithm for the computation of spherical harmonic coefficients for a polyhedral source, where the integrals defining the coefficients are obtained through a recursion scheme. Tsoulis et al. (2009) elaborated the method demonstrating its numerical instability after degree 60. Jamet and Tsoulis (2020) developed a line integral method for the same computation, where the three-dimensional integral describing

the spherical harmonic coefficients is decomposed into two parts, one perpendicular and one parallel to each face of the polyhedral source. Each of the two parts is an independent triple integral which is transformed into a summation of surface integrals over the polyhedral faces and eventually into a summation of line integrals along the polyhedral edges, the latter being solved using Romberg's method. A similar decomposition of the position vector into a parallel and an orthogonal part is carried out in D'Urso (2015), where the gravitational potential expression is solved analytically using linear varying density and applied to a right rectangular prism.

The interest for the numerical implementation and performance of the aforementioned techniques is relevant to a wide array of applications, including among others topographic and isostatic models (Rummel et al. 1988), asteroid dynamic modeling (Werner and Scheeres 1997; Takahashi and Scheeres 2014), spherical, spheroidal and ellipsoidal gravity field approximations (Hu and Jekeli 2015).

The present study focuses on the numerical implementation and comparison of the approaches proposed by Werner (1997) and Jamet and Tsoulis (2020). The analysis attempts to quantify specific numerical aspects linked to these methodologies, namely (a) their spectral characteristics, (b) their convergence behavior, especially regarding the location of the computation point with respect to the corresponding sphere of convergence, namely the Brillouin sphere, and (c) their agreement against the analytical solution.

In Sect. 2, the underlying theory of the considered methodologies is outlined. Section 3 documents their numerical implementation considering the real shape data of asteroids Eros and Didymos. After some statistical indicators for the calculated sets of spherical harmonic coefficients are computed, the extracted gravitational potential of these coefficients is compared to the analytical solution. In a first scenario, the computation of the gravitational potential is carried out at arbitrary points creating a 3D grid around the asteroids, a second setup considers computation at points with an increasing distance from the center of mass of the corresponding body, while a final test considers an evaluation at fixed points for an increasing degree expansion.

## 2 Theory

The basic equation is the definition of the gravitational potential function due to a finite three-dimensional mass distribution with constant mass density  $\rho$

$$V = G\rho \iiint_U \frac{dU(Q)}{l}, \quad (1)$$

where  $G$  is the Newtonian gravitational constant,  $U$  the volume and  $l$  the distance between the computation point and the infinitesimal volume element  $dU$  at the integration point  $Q$ .

The numerical methods for the evaluation of Eq. (1) that are going to be considered here are based on the computation of the spherical harmonic coefficients  $C_{n,m}$ ,  $S_{n,m}$  which enter the gravitational potential expression in an infinite harmonic series (Heiskanen and Moritz 1967)

$$V(r, \theta, \lambda) = \frac{GM}{r} \left\{ 1 + \sum_{n=1}^{+\infty} \left( \frac{a}{r} \right)^n \sum_{m=0}^n P_{n,m}(\cos\theta) [C_{n,m} \cos(m\lambda) + S_{n,m} \sin(m\lambda)] \right\}, \quad (2)$$

where  $(r, \theta, \lambda)$  are the spherical coordinates of the computation point,  $M$  the total mass of the solid body,  $a$  the radius of a sphere centered at the origin of the spherical coordinate system, usually selected to have a minimum value so that the resulting sphere can enclose all gravitating masses, and  $P_{n,m}$  the Legendre functions.

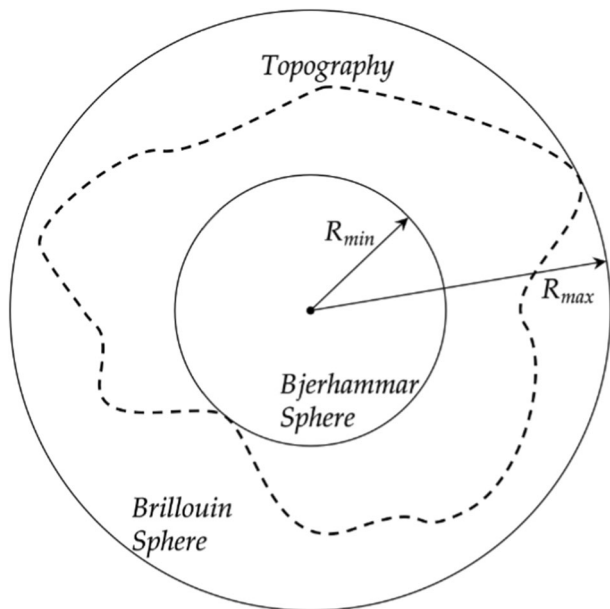
The radius  $a$  is linked with the definition of two special spheres, the Brillouin and the Bjerhammar sphere. The Brillouin sphere is a theoretical sphere with its center placed at the distribution's center of mass and a radius selected so that the sphere can enclose the entire mass allocation. Accordingly, the Bjerhammar sphere, also with its center placed at the center of mass, has a maximum radius value so that the sphere resides completely inside the mass distribution without intersecting its boundary (Fig. 1). The definition of these spheres is important as they are inextricably linked to the numerical convergence of the aforementioned series expansion for the gravitational potential function. The goal of present paper is to investigate this convergence behavior inside and near the boundaries of the Brillouin sphere.

In the following, the aforementioned considered methods are briefly outlined. The examined homogeneous mass distribution will be always the one defined by a closed polyhedral finite triangulation with a constant density value.

## 2.1 The Line Integral Approach for Spherical Harmonic Coefficients

The method by Jamet and Tsoulis (2020) aims at the calculation of the spherical harmonic coefficients of Eq. (2) in an analytical way without using any recursive relations. There are no prerequisites or restrictions regarding the geometry of the examined solid body. Thus, the polyhedron's faces can be created by a different number of vertices. The polyhedral source is divided into smaller polyhedra, each one being defined by one face of the whole

**Fig. 1** Definition of Brillouin and Bjerhammar spheres



polyhedron and the origin of the coordinate system, while the calculations take place for each smaller polyhedron separately. The origin of the coordinate system can be placed anywhere in 3D space, not necessarily at the polyhedron's center of mass. All the involved geometric parameters derived from the polyhedron definition are shown in Fig. 2.

The coefficients of Eq. (2) are then defined as Werner (1997) and Heiskanen and Moritz (1967)

$$\begin{bmatrix} C_{n,m} \\ S_{n,m} \end{bmatrix} = \frac{2 - \delta_{0,m} (n-m)!}{Ma^n (n+m)!} \rho \iiint_U \begin{bmatrix} h_{n,m}^C(Q) \\ h_{n,m}^S(Q) \end{bmatrix} dU(Q), \quad (3)$$

where  $\delta_{0,m}$  is the Kronecker delta function, which equals to 0 if  $m \neq 0$  and to 1 if  $m = 0$ ,  $\frac{\rho}{M}$  is defining the total volume of the mass distribution and  $h_{n,m}^C, h_{n,m}^S$  are given by

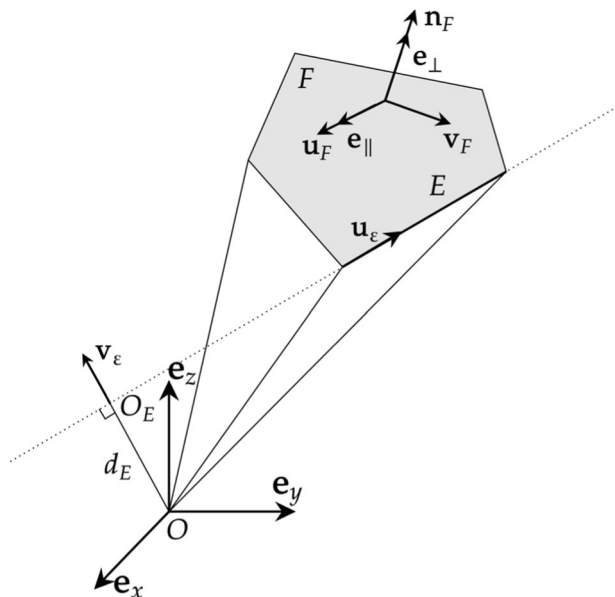
$$h_{n,m}^C(r', \theta', \lambda') = r'^n P_{n,m}(\cos \theta') \cos(m\lambda'), \quad (4)$$

$$h_{n,m}^S(r', \theta', \lambda') = r'^n P_{n,m}(\cos \theta') \sin(m\lambda'). \quad (5)$$

Thus, the problem of the coefficients' computation is transferred to the calculation of the integral  $\iiint_U h_{n,m}(Q) du$ . Tsoulis et al. (2009), using the Gauss theorem, transform this volume integral into a summation of surface integrals referring to each face of the polyhedron as

$$\iiint_U h_{n,m}(Q) du = \frac{1}{n+3} \sum_{F \in \partial U} d_F \iint_F h_{n,m} dS, \quad (6)$$

**Fig. 2** Geometric parameters for a single polyhedron division on the line integral approach



where  $F$  denotes a face of the polyhedron,  $dS$  is the infinitesimal vector area and  $d_F$  the minimal orthogonal distance of the origin of the coordinate system to this planar face.

The problem is now reduced to the computation of the surface integral

$$I_{n,m} = \iint_F h_{n,m} dS. \quad (7)$$

For the transformation of the above surface integral into line integrals, the Kelvin–Stokes theorem is used, while taking into account that

$$\nabla h_{n+1,m} \cdot \mathbf{e}_z = (n + m + 1)h_{n,m}. \quad (8)$$

Vector  $\mathbf{e}_z$  is decomposed into two parts, one perpendicular  $\mathbf{e}_\perp$  and one parallel  $\mathbf{e}_\parallel$  to the face under examination, according to the vector addition

$$\mathbf{e}_z = \mathbf{e}_\perp + \mathbf{e}_\parallel. \quad (9)$$

These vectors can be also expressed as

$$\mathbf{e}_\perp = (\mathbf{e}_z \cdot \mathbf{n}_F) \mathbf{n}_F, \quad (10)$$

$$\mathbf{e}_\parallel = (\mathbf{n}_F \times \mathbf{e}_z) \times \mathbf{e}_z, \quad (11)$$

where  $\mathbf{n}_F$  is the outward normal unit vector to each face of the polyhedron.

Thus, the integral in Eq. (7) is now equivalent to

$$I_{n,m} = \frac{1}{n + m + 1} (I_{n,m\perp} + I_{n,m\parallel}), \quad (12)$$

where

$$I_{n,m\parallel} = \iint_F \nabla h_{n+1,m} \cdot \mathbf{e}_\parallel dS, \quad (13)$$

$$I_{n,m\perp} = \iint_F \nabla h_{n+1,m} \cdot \mathbf{e}_\perp dS. \quad (14)$$

After the application of the Stokes theorem and the use of some mathematical equivalences, Eq. (13) can be expressed as

$$I_{n,m\parallel} = \sum_{E \in \partial F} [\mathbf{n}_F, \mathbf{e}_z, \mathbf{u}_E] \int_E h_{n+1,m} dL, \quad (15)$$

where  $E$  is one edge on each face of the polyhedron,  $[\mathbf{n}_F, \mathbf{e}_z, \mathbf{u}_E]$  is the triple product between these vectors and  $\mathbf{u}_E$  the normal unit vector along edge  $E$ . Accordingly, for the perpendicular part Eq. (14) can now be written as

$$I_{n,m\perp} = \frac{(\mathbf{e}_z \cdot \mathbf{n}_F)}{n + 2} \sum_{E \in \partial F} d_E \int_E \nabla h_{n+1,m} \cdot (\mathbf{v}_E \times \mathbf{u}_E) dL \quad (16)$$

where  $d_E$  is the distance of the line bearing the edge  $E$  from the origin of the coordinate system (Fig. 2) and  $\mathbf{v}_E$  the normal unit vector along this direction.

The line integrals of expressions (15) and (16), which refer to every edge of every face of the polyhedral mass distribution, are solved numerically using Romberg's integration method.

The transformation of the evaluated spherical harmonic coefficients to their normalized counterpart takes place via the standard expression

$$\begin{bmatrix} \bar{C}_{n,m} \\ \bar{S}_{n,m} \end{bmatrix} = \begin{bmatrix} C_{n,m}/N_{n,m} \\ S_{n,m}/N_{n,m} \end{bmatrix}, \quad (17)$$

where  $N_{n,m}$  is the normalization factor (Heiskanen and Moritz 1967)

$$N_{n,m} = \sqrt{(2 - \delta_{0,m})(2n+1) \frac{(n-m)!}{(n+m)!}} \quad (18)$$

and  $\delta_{0,m}$  is the Kronecker delta function.

## 2.2 Werner's Method for Spherical Harmonic Coefficients

Werner (1997) computes the spherical harmonic coefficients recursively. In this case, the hull of the polyhedron under study must be defined exclusively by triangular faces, unlike the aforementioned line integral approach where also polygonal faces can be used. Each one of the faces defines a tetrahedron with respect to the origin of the coordinate system and in this way the polyhedral volume is divided into individual tetrahedra.

The computation scheme is based on the equation

$$\begin{bmatrix} C_{n,m} \\ S_{n,m} \end{bmatrix} = \iiint_{\text{polyhedron}} \begin{bmatrix} c_{n,m} \\ s_{n,m} \end{bmatrix} dm, \quad (19)$$

where

$$\begin{bmatrix} c_{n,m} \\ s_{n,m} \end{bmatrix} = \frac{1}{M} (2 - \delta_{0,m}) \frac{(n-m)!}{(n+m)!} \left( \frac{r'}{a} \right)^n P_{n,m}(\cos \theta') \begin{bmatrix} \cos m\lambda' \\ \sin m\lambda' \end{bmatrix}. \quad (20)$$

The proposed recurrence equations for the computation of the fully normalized integrands  $\bar{c}_{n,m}$  and  $\bar{s}_{n,m}$  are

$$n = m = 0 : \begin{bmatrix} \bar{c}_{0,0} \\ \bar{s}_{0,0} \end{bmatrix} = \frac{1}{M} \begin{bmatrix} 1 \\ 0 \end{bmatrix}, \quad (21)$$

$$n = m = 1 : \begin{bmatrix} \bar{c}_{1,1} \\ \bar{s}_{1,1} \end{bmatrix} = \frac{1}{\sqrt{3}M} \frac{1}{a} \begin{bmatrix} x' \\ y' \end{bmatrix}, \quad (22)$$

$$n = m > 1 : \begin{bmatrix} \bar{c}_{n,n} \\ \bar{s}_{n,n} \end{bmatrix} = \frac{2n-1}{\sqrt{2n(2n+1)}} \frac{1}{a} \begin{bmatrix} x' & -y' \\ y' & x' \end{bmatrix} \begin{bmatrix} \bar{c}_{n-1,n-1} \\ \bar{s}_{n-1,n-1} \end{bmatrix} \quad (23)$$

$$\begin{bmatrix} \bar{c}_{n,m} \\ \bar{s}_{n,m} \end{bmatrix} = (2n-1) \sqrt{\frac{2n-1}{(2n+1)(n+m)(n-m)}} \frac{z'}{a} \begin{bmatrix} \bar{c}_{n-1,m} \\ \bar{s}_{n-1,m} \end{bmatrix} - \sqrt{\frac{(2n-3)(n+m-1)(n-m-1)}{(2n+1)(n+m)(n-m)}} \left( \frac{r'}{a} \right)^2 \begin{bmatrix} \bar{c}_{n-2,m} \\ \bar{s}_{n-2,m} \end{bmatrix}, \quad (24)$$

$$\begin{bmatrix} \bar{c}_{n,n-1} \\ \bar{s}_{n,n-1} \end{bmatrix} = \frac{2n-1}{\sqrt{2n+1}} \frac{z'}{a} \begin{bmatrix} \bar{c}_{n-1,n-1} \\ \bar{s}_{n-1,n-1} \end{bmatrix}. \quad (25)$$

The philosophy of this method is to change the used coordinate variables  $x', y', z'$  and express them as trinomials with respect to the new ones  $X, Y, Z$ . Thus, for a given tetrahedron the following 3 trinomials are used

$$x'(X, Y, Z) = x_1 X + x_2 Y + x_3 Z, \quad (26)$$

$$y'(X, Y, Z) = y_1 X + y_2 Y + y_3 Z, \quad (27)$$

$$z'(X, Y, Z) = z_1 X + z_2 Y + z_3 Z, \quad (28)$$

with  $x_1, x_2, x_3, y_1, y_2, y_3, z_1, z_2, z_3$  the Cartesian coordinates of the 3 vertices on one triangular face. After this change, the coefficients  $\bar{c}_{n,m}, \bar{s}_{n,m}$  are still homogeneous polynomials of degree  $n$  as before, but in terms of the new variables  $X, Y, Z$  according to

$$\begin{bmatrix} \bar{c}_{n,m}(x', y', z') \\ \bar{s}_{n,m}(x', y', z') \end{bmatrix} \rightarrow \begin{bmatrix} \bar{c}_{n,m}(X, Y, Z) \\ \bar{s}_{n,m}(X, Y, Z) \end{bmatrix} = \sum_{i+j+k=n} \begin{bmatrix} \bar{\alpha}_{i,j,k} \\ \bar{\beta}_{i,j,k} \end{bmatrix} X^i Y^j Z^k. \quad (29)$$

The summation shown in (29) runs through all possible combinations of non-negative integers for the values of  $i, j, k$ , provided  $i + j + k = n$ , while the symbols  $\bar{\alpha}_{i,j,k}, \bar{\beta}_{i,j,k}$  are in fact the trinomial coefficients of  $X, Y, Z$  as presented in Eqs. (26)–(28). Using the following integral solution (Lien and Kajiya 1984)

$$\iiint X^i Y^j Z^k dX dY dZ = \frac{i!j!k!}{(i+j+k+3)}, \quad (30)$$

the final equation for the fully normalized spherical harmonic coefficients according to Werner (1997) becomes

$$\begin{bmatrix} \bar{C}_{n,m} \\ \bar{S}_{n,m} \end{bmatrix} = \rho \sum_{\text{tetrahedra}} \left( \frac{\det J}{(n+3)!} \sum_{i+j+k=n} i!j!k! \begin{bmatrix} \bar{\alpha}_{i,j,k} \\ \bar{\beta}_{i,j,k} \end{bmatrix} \right), \quad (31)$$

where  $\det J$  is the determinant of the Jacobian matrix which follows straight forward from (26)–(29)

$$J = \begin{bmatrix} x_1 & x_2 & x_3 \\ y_1 & y_2 & y_3 \\ z_1 & z_2 & z_3 \end{bmatrix}. \quad (32)$$

### 2.3 Analytical Solution

The line integral analytical algorithm for the gravity field of a generally shaped polyhedron is an analytical methodology which provides closed exact formulas for the direct computation of the gravitational potential as well as its first- and second-order derivatives. It requires a subsequent forward application of Gauss's divergence theorem that demands a rigorous monitoring of the computation point and its projections onto the



polyhedral planes of the faces and the segments of each face, in order to properly account for the involved numerical singularities (Petrović 1996; Tsoulis and Petrović 2001; Tsoulis 2012).

The advantage of the technique, as any other analytical formalism, is that it allows the computation point to be placed anywhere in three-dimensional space outside the mass distribution, even inside the Brillouin sphere, being aware of the numerical singularities.

The approach is based on the application of the Gauss divergence theorem in Eq. (1), which transforms the volume integral into a summation of surface integrals. A subsequent application of the divergence theorem on the obtained surface integrals leads to a summation of line integrals defined along polyhedral edges. The final equations, which are presented below, consist of a double summation running through every segment and every face of the polyhedral source.

$$V = \frac{G\rho}{2} \sum_{p=1}^n \sigma_p h_p \left[ \sum_{q=1}^m \sigma_{pq} h_{pq} LN_{pq} + h_p \sum_{q=1}^m \sigma_{pq} AN_{pq} + SING_{A_p} \right], \quad (33)$$

$$\mathbf{V}_i = G\rho \sum_{p=1}^n \cos(\mathbf{N}_p, \mathbf{e}_i) \left[ \sum_{q=1}^m \sigma_{pq} h_{pq} LN_{pq} + h_p \sum_{q=1}^m \sigma_{pq} AN_{pq} + SING_{A_p} \right] \mathbf{e}_i, \quad (34)$$

$$V_{ij} = G\rho \sum_{p=1}^n \cos(\mathbf{N}_p, \mathbf{e}_i) \left[ \sum_{q=1}^m \cos(\mathbf{n}_{pq}, \mathbf{e}_j) LN_{pq} + \sigma_p \cos(\mathbf{N}_p, \mathbf{e}_j) \sum_{q=1}^m \sigma_{pq} AN_{pq} + SING_{B_{pj}} \right], \quad (35)$$

for  $i, j = x, y, z$ , where

$$LN_{pq} = \ln \left( \frac{s_{2pq} + l_{2pq}}{s_{1pq} + l_{1pq}} \right) \quad (36)$$

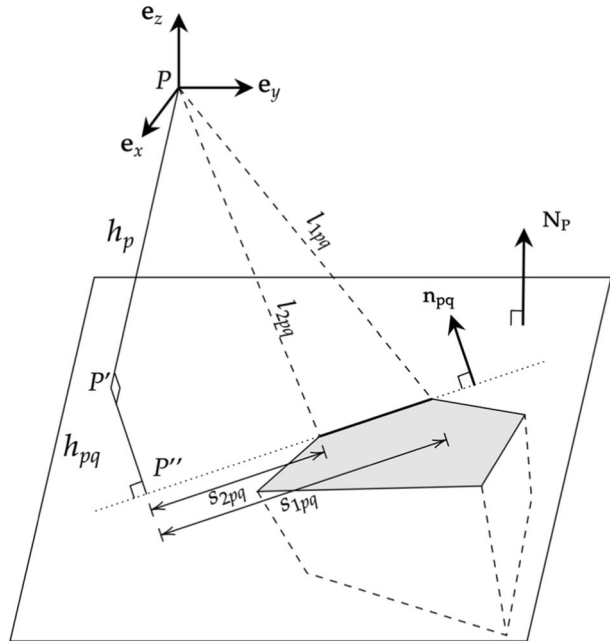
$$AN_{pq} = \arctan \left( \frac{h_p s_{2pq}}{h_{pq} l_{2pq}} \right) - \arctan \left( \frac{h_p s_{1pq}}{h_{pq} l_{1pq}} \right), \quad (37)$$

and  $SING_{A_p}$ ,  $SING_{B_{pj}}$  are singular terms which are calculated only at specific positions of the computation point and its projections with respect to the mass distribution. All other parameters involved in these equations are presented in Fig. 3 and express geometric quantities that are explained in detail in Tsoulis and Gavriilidou (2021).

### 3 Numerical Implementation

The methodology of the line integral approach by Jamet and Tsoulis (2020) (cf. Section 2.1) has been applied to the real shape data of two asteroids, Eros and Didymos, and compared with Werner's method, summarized in Sect. 2.2. These asteroids have been chosen due to their particular shape, specifically the former due to its irregularity while the latter due to its almost sphericity. The spherical harmonic coefficients for the gravitational potential of the asteroids have been calculated up to the degree and order 100 by

**Fig. 3** Geometrical parameters involved in the final equations of the general polyhedron method



both approaches, while the obtained gravitational potential by these two sets of coefficients has been compared against the precise analytical solution of the line integral algorithm, explained in Sect. 2.3. The maximum degree of expansion was chosen to be 100 for efficiency of the implemented codes, as the required CPU time was increasing exponentially.

An independent orthonormal Cartesian coordinate system placed at the center of mass is defined for each asteroid separately, where the selection of the three axes is adopted by the used shape models.

In the sequel, the methodology of Jamet and Tsoulis (2020) will be described as method A, the approach proposed by Werner (1997) as method B and the line integral analytical solution for the gravity signal of an arbitrarily shaped polyhedron as method C.

### 3.1 Eros

The main and primary source of information about the first examined asteroid 433 Eros (Fig. 4) is the NASA's Near Earth Asteroid Rendezvous (NEAR) discovery mission. NEAR went into orbit around this near Earth asteroid in December 1998 and has provided data for its shape, rotation and gravity field. The shape model of Eros has been derived from the procession of the NEAR laser rangefinder (NLR) data by the Multi-Spectral Imager team of the mission. It is represented in the basis of surface spherical harmonic up to degree and order 24 (Miller et al. 2002). The shape model can be found at Nasa's PDS Small Bodies Node "<https://sbn.psi.edu/pds/shape-models/>".

The entire calculated volume equals 2491.6 km<sup>3</sup>, the mass density is set up to 2670 kg/m<sup>3</sup> and the gravitational constant  $G$  has the value 6.67408E-11 m<sup>3</sup>/(kg s<sup>2</sup>). The radius of the Brillouin, Bjerhammar and the mean sphere of all asteroid vertices with respect to the origin of the Cartesian coordinate system placed exactly at the asteroid's center of mass

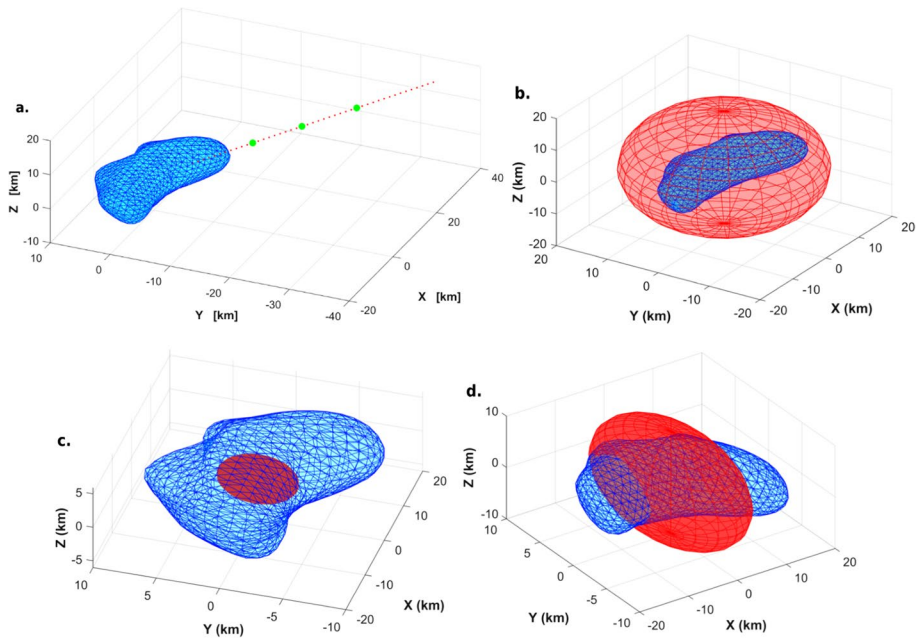


**Fig. 4** Asteroid Eros in blue color and **(b)** Brillouin sphere, **(c)** Bjerhammar sphere and **(d)** mean radius sphere in red color. Also, **(a)** the 45 computation points (red dots) with the three selected (green dots) and their position in the 3D space with respect to the asteroid

are shown in Table 1. The irregular shape of Eros is reflected on the significant difference in the radii of the two spheres, thus defining a wide region of uncertainty for the two spherical harmonic methodologies (Fig. 4).

The used CPU time for both methodologies is listed in Table 1. Method A is implemented on Jupyter Notebook while methods B and C on MATLAB. The absolute differences of the spherical harmonic coefficients  $\bar{C}_{nm}$  and  $\bar{S}_{nm}$  derived from the two spherical harmonic methodologies are smaller than  $1\text{E-}9$ , while the obtained rms equals to  $6.5\text{E-}11$  for  $\bar{C}_{nm}$  and  $5.7\text{E-}11$  for  $\bar{S}_{nm}$ . The highest numerical differences are found in the highest degrees proportionally.

A spectral assessment took place in order to evaluate the statistical behavior of the spherical harmonic coefficients of methods A and B by the calculation of various indicators (Tsoulis and Patlakis 2013). The degree variance  $\sigma_n^2$  which indicates the total signal power for evolving degree  $n$  and the order variance  $\sigma_m^2$  referring to the order  $m$  were computed for both sets of coefficients according to

**Table 1** Computational and geometrical information about the two examined asteroids

Asteroid	Bjerhammar radius (km)	Mean radius (km)	Brillouin radius (km)	Number of vertices	Number of faces	CPU time for method A	CPU time for B
Eros	3.2189	9.9240	17.6481	856	1708	5 h 34 min	1 h 49 min
Didymos	0.3523	0.3925	0.4275	1000	1996	5 h 50 min	2 h 7 min

$$\sigma_n^2 = \sum_{m=0}^n (\bar{C}_{nm}^2 + \bar{S}_{nm}^2), \quad (38)$$

$$\sigma_m^2 = \sum_{n=m}^{n_{\max}} (\bar{C}_{nm}^2 + \bar{S}_{nm}^2). \quad (39)$$

The square root of these quantities defines the square root of degree and order variance, respectively. The square root of degree and order variance's rms for method B are both equal to 9.989E-2 while method A has a higher rms value by 1.5E-15.

The absolute differences of these variances have been calculated as

$$D_n = |\sigma_n^A - \sigma_n^B|, \quad (40)$$

$$D_m = |\sigma_m^A - \sigma_m^B|, \quad (41)$$

where  $\sigma_n^A, \sigma_m^A$  are the square root of degree and order variances, respectively, for method A and  $\sigma_n^B, \sigma_m^B$  the computed square root of variances for method B.

The relative measure of difference degree variance (42) and difference order variance (43), was also calculated as follows,

$$\Delta\sigma_n^2 = \sum_{m=0}^n (\Delta\bar{C}_{nm}^2 + \Delta\bar{S}_{nm}^2), \quad (42)$$

$$\Delta\sigma_m^2 = \sum_{l=m}^{n_{\max}} (\Delta\bar{C}_{lm}^2 + \Delta\bar{S}_{lm}^2), \quad (43)$$

while the square root of these quantities defines the square root of difference degree and order variances, respectively.

The computed square root of degree  $\sigma_n$  and order  $\sigma_m$  variances for both spherical harmonic methodologies, their absolute differences  $D_n, D_m$  and the corresponding square root of difference degree  $\Delta\sigma_n$  and order  $\Delta\sigma_m$  variances are shown in Fig. 5. An additional window was inserted on the upper panel of Fig. 5 showing the contribution of the highest degrees. The square root of degree and order variances of the two methodologies seem to be almost identical as they have small value differences. Considering the square root of difference degree and order variances it seems that the spherical harmonic coefficients have greater variations in terms of degree.

The statistical indicators min, max, mean and rms for the absolute differences of square root variances (40), (41) between the two methods, as well as the square root of difference order and degree variances are presented in Table 2.

The differences in the square root of degree variance between the two methods are ranging from 0 to 8E-10 and in square root of order variance from 2E-16 to 8.6E-10. The rms of those differences is 3.7E-10 and 4.1E-10 for square root of degree and order variance, respectively. Concerning the square root of difference degree variances, they range between 0 and 1.4E-09, while the square root of difference order variances between 5.9E-11 and 1.2E-9. Their calculated rms is the same for both cases.

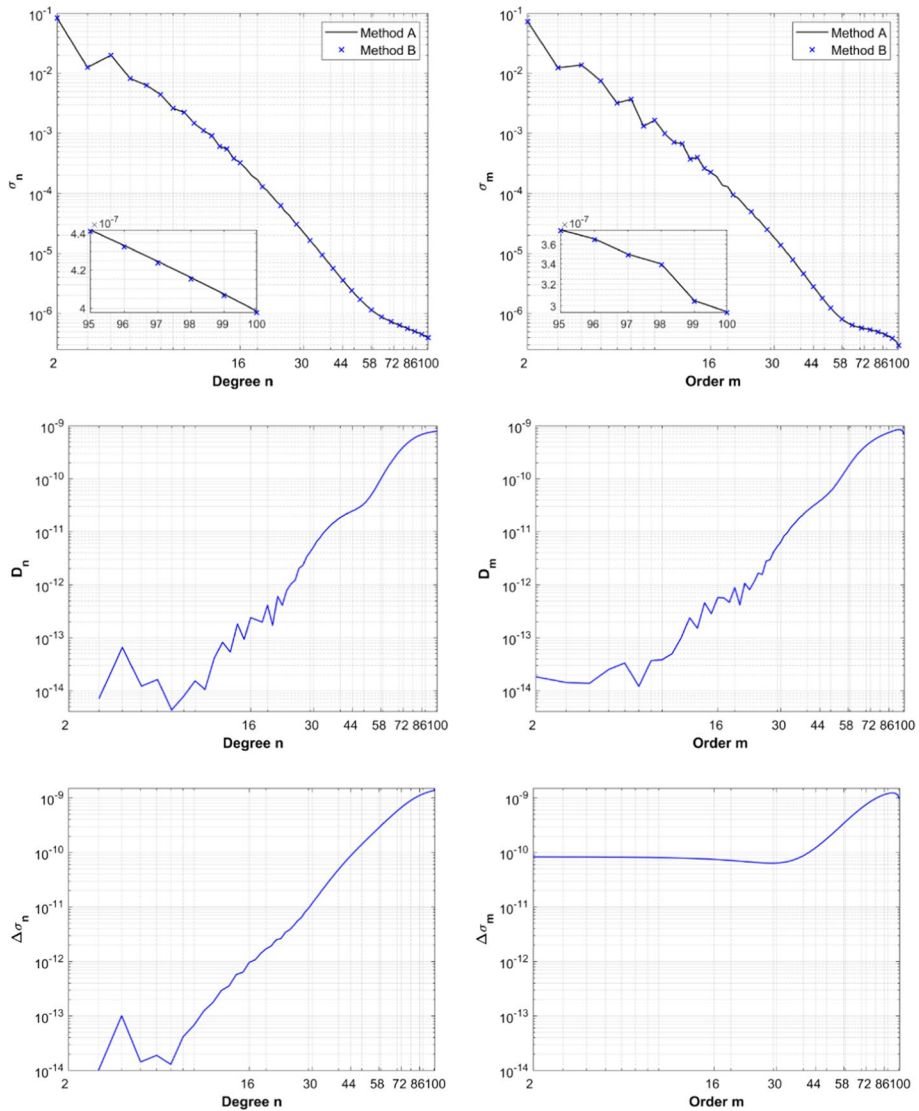


**Fig. 5** Potential coefficient spectra of the two examined methodologies for asteroid Eros, in logarithmic scale. Upper panel: square root of degree (left) and order (right) variances. Middle panel: absolute differences of square root degree and order variances. Lower panel: square root of difference degree and order variances

Another relative measure for the direct comparison between the two sets of coefficients is the correlation by degree  $\rho_n$  and the correlation by order  $\rho_m$ . This measure gives a strong indication of whether the two coefficients sets are correlated and up to which degree and order. The corresponding definitions read

**Table 2** Statistical indicators for the absolute differences of the square root degree variances, absolute differences of the square root order variances, square root of difference degree variances and square root of difference order variances, derived from methods A and B for asteroid Eros

	[D <sub>n</sub> ]	[D <sub>m</sub> ]	[Δσ <sub>n</sub> ]	[Δσ <sub>m</sub> ]
Min	0	2.2204E-16	0	5.8974E-11
Max	8.0104E-10	8.6317E-10	1.3775E-09	1.2385E-09
Mean	2.2772E-10	2.6417E-10	4.0048E-10	4.4040E-10
Rms	3.6864E-10	4.0990E-10	6.1725E-10	6.1725E-10

$$\rho_n = \frac{\sum_{m=0}^n (\bar{C}_{nm}^A \bar{C}_{nm}^B + \bar{S}_{nm}^A \bar{S}_{nm}^B)}{\sqrt{\sigma_n^2(\bar{C}_{nm}^A, \bar{S}_{nm}^A) \sigma_n^2(\bar{C}_{nm}^B, \bar{S}_{nm}^B)}}, \quad (44)$$

$$\rho_m = \frac{\sum_{n=m}^{n_{\max}} (\bar{C}_{nm}^A \bar{C}_{nm}^B + \bar{S}_{nm}^A \bar{S}_{nm}^B)}{\sqrt{\sigma_m^2(\bar{C}_{nm}^A, \bar{S}_{nm}^A) \sigma_m^2(\bar{C}_{nm}^B, \bar{S}_{nm}^B)}}, \quad (45)$$

where  $\bar{C}_{nm}^A, \bar{S}_{nm}^A$  are the spherical harmonic coefficients for method A and  $\bar{C}_{nm}^B, \bar{S}_{nm}^B$  for method B,  $\sigma_n^2(\bar{C}_{nm}^A, \bar{S}_{nm}^A), \sigma_n^2(\bar{C}_{nm}^B, \bar{S}_{nm}^B)$  the degree variance (38) for method A and B, respectively, and  $\sigma_m^2(\bar{C}_{nm}^A, \bar{S}_{nm}^A), \sigma_m^2(\bar{C}_{nm}^B, \bar{S}_{nm}^B)$  the order variance (39).

The calculated correlation between method A and B is presented in Fig. 6. The two methods agree at 100% and have correlation by degree equal to 1 up to degree 45 and correlation by order equal to 1 up to order 42. From there on, the correlation decreases to 99.9996% by degree and 99.9998% by order.

A further spectral assessment tool is the smoothing per degree  $S_n$  and smoothing per order  $S_m$  which are defined as

$$S_n = \frac{\sum_{m=0}^n (\Delta \bar{C}_{nm}^2 + \Delta \bar{S}_{nm}^2)}{\sigma_n^2(\bar{C}_{nm}^B, \bar{S}_{nm}^B)}, \quad (46)$$

$$S_m = \frac{\sum_{n=m}^{n_{\max}} (\Delta \bar{C}_{nm}^2 + \Delta \bar{S}_{nm}^2)}{\sigma_m^2(\bar{C}_{nm}^B, \bar{S}_{nm}^B)}, \quad (47)$$

where the degree and order variances refer here to method B.

Quantities (46) and (47), shown in Fig. 7, express the degree of smoothing obtained if the model of method A is subtracted from the one of method B. The two approaches seem to fit with the smoothing increasing linearly. Specifically, the smoothing ranges from 0 to 1.2E-5 per degree and from 3.5E-21 to 1.1E-5 per order.

The gravitational potential obtained by the spherical harmonic coefficients of methods A and B was evaluated for different setups and compared with method C directly in the space domain, in order to evaluate the performance of the two models in spherical harmonic synthesis.

The first scenario was the computation of the gravitational potential at 5103 arbitrary points in the space surrounding the mass distribution, which were normally distributed creating a 3D grid. The grid in question consists of 7 planes in total (Fig. 8), each of them defined by 27 points in the z- and y-axis, ranging from -52 to 52 km with respect to the

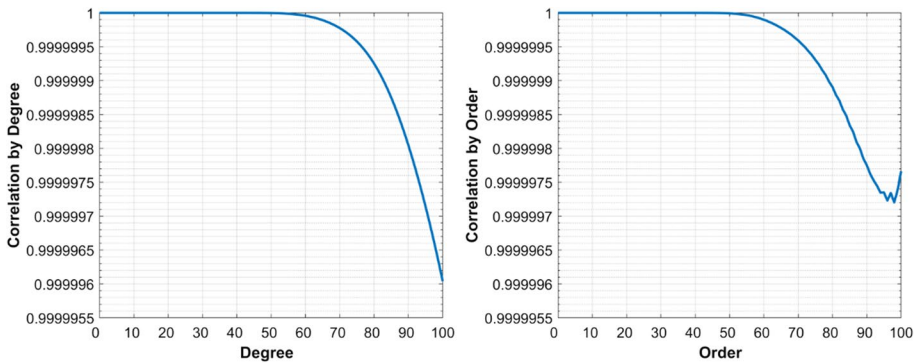


**Fig. 6** (left) Correlation by degree and (right) correlation by order in logarithmic scale between the two sets of fully normalized spherical harmonic coefficients

center of mass. The  $x$  coordinate was set constant for all points at one plane and equal to the values  $-30, -20, -10, 0, 10, 20$  and  $30$  km for the 7 planes, respectively. The obtained results are shown in Fig. 9, where the first column illustrates the gravitational potential from method A, the second column gives the differences with method B and the last column the differences with method C.

The potential decreases as the computation point moves away from the attracting mass with a small exception at the planes that fall inside the asteroid (planes 3, 4, 5). There, when one approaches the Brillouin sphere, the value of the potential is much higher than at adjacent points. The differences in the gravitational potential for the two spherical harmonic methods are smaller as the computation point approaches the solid body, except for some non-convergence areas very close to the mass. The differences with the potential derived from method C are much more significant than the corresponding differences for the two spherical harmonic methods with some areas of higher numerical deviations appearing due to the asteroid's shape. Some points close to the mass distribution where the calculated gravitational potential was not converging, thus having significant differences

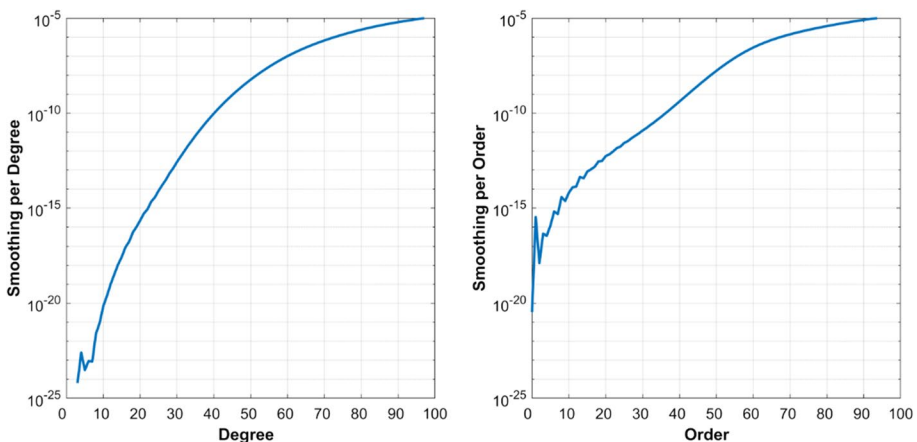


**Fig. 7** (left) Smoothing per degree and (right) smoothing per order in logarithmic scale

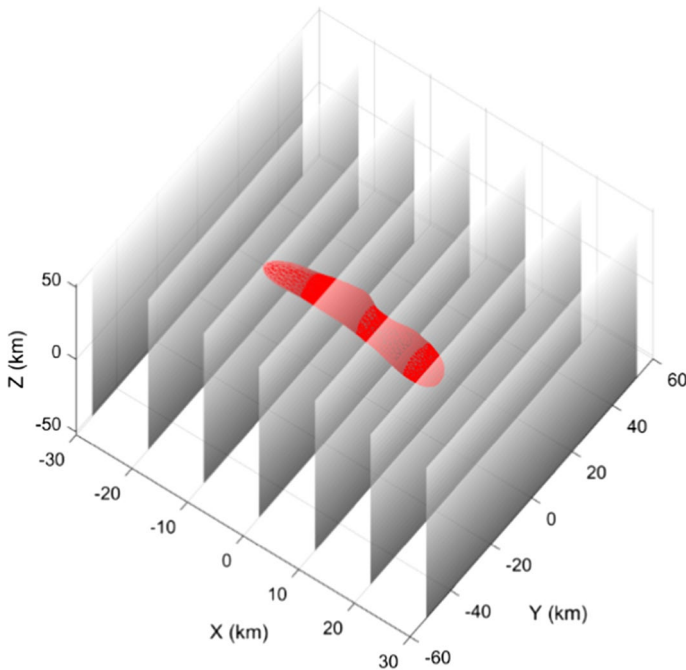


**Fig. 8** 2D planes for the computation of gravitational potential with respect to the asteroid Eros

from the nearby points, have been excluded from the process, limiting the investigation area near the boundary of Brillouin sphere.

For the non-convergence areas at planes 3, 4, 5, it can be noted that the maximum differences between methods A and B (second column of Fig. 9) are 0.06, 7 and 0.06  $\text{m}^2/\text{s}^2$ , respectively, while between methods A and C 15, 45 and 15  $\text{m}^2/\text{s}^2$  for the same planes. Thus, the differences at the non-convergence area between method A and C are 250 times the corresponding difference between method A and B for planes 3 and 5, while for plane 4 the same difference relation equals 6.5 times.

At the areas near the edges of the 2D grid, the differences between method A and B are about  $1\text{E-}15$  while between method A and C the differences are of the order of  $1\text{E-}12$  for planes 4–7 and  $1\text{E-}3$  for planes 1–3.

Two questions remain to be addressed after this 3D modeling and comparison between the three methods. First, the contribution in the gravitational potential of the relative position of the computation point with respect to the mass for a fixed value of spherical harmonic degree expansion and secondly the convergence of the gravitational potential for varying degree expansion at one constant computation point at a time. These are essentially the two factors that influence the accuracy of the gravitational results for a specific methodology and a known regarded polyhedron, namely the degree expansion of the series and the exact position of the computation point with respect to the mass distribution.

For the first case, the gravitational potential for  $k = \{1, 2, \dots, 45\}$  computation points (Fig. 4) was calculated from methods A and B. All points  $P_k$  have the same values for the  $\theta_k$  and  $\lambda_k$  coordinates as given in Table 4, while the only parameter changing is the distance  $r_k$  from the center of the coordinate system:  $r_k = 7087.2 \text{ km} + (k - 1) * 1000 \text{ m}$ .



The gravitational potential was computed at each point  $P_k$  with varying degree  $n = \{5, 10, 20, 100\}$  for both methods A and B. These solutions were also compared with the results of the closed analytical method C.

The absolute differences in the gravitational potential for the four sets of numerical solutions between the 3 examined methods are depicted in logarithmic scale in Fig. 10. The first diagram shows the differences between methods A and C, the second one the differences between methods A and B. The blue line indicates the Brillouin sphere.

An important remark is the fact that the first 11 points lie within the Brillouin sphere, which is where the greatest deviation in the results is noted as expected. At these points it seems that the sets with the highest degree of expansion have proportionally the largest differences (Table 3), as they are affected by the factor  $(a/r)^n$ . For example, at  $P_1$  the difference between methods A and C for  $n=100$  is  $4E+34 \text{ m}^2/\text{s}^2$ , for  $n=20$  is  $7E+5 \text{ m}^2/\text{s}^2$ , for  $n=10$  it reduces to  $1E+3 \text{ m}^2/\text{s}^2$  and for  $n=5$  it reaches  $4 \text{ m}^2/\text{s}^2$ . The same applies to the rest of the points, while as the computation point reaches the boundary of the Brillouin sphere those differences are getting smaller. About 3.5 km inside the Brillouin sphere methods A and C differ numerically at the  $1E-1$  level for  $n = \{5, 10\}$ , about 2.5 km the difference becomes  $1E-2$  for  $n=20$  and about 500 m the difference equals  $1E-5$  for  $n=100$ .

The solutions A and B are very similar inside the Brillouin sphere and agree at a  $1E-10$ ,  $1E-7$  and  $1E-2$  level for  $n = \{5, 10, 20\}$ , respectively, while for  $n=100$  the level of agreement becomes  $1E-2$  about 2.5 km inside the boundary of the sphere ( $P_9, P_{10}, P_{11}$ ). In most points for degrees  $n = \{10, 100\}$  method A is closer to method C than method B, specifically for 7 of 11 and 8 of 11, respectively.

Outside the Brillouin sphere, at points  $k = \{12, 13, \dots, 45\}$ , the solutions with the highest degree of expansion converge to the analytical solution more quickly than the other sets. The differences between the two spherical harmonic analysis methods are much smaller compared to the analytical solution with some values even equal numerically to  $0 \text{ m}^2/\text{s}^2$  (Fig. 10). The points having nonzero differences are found close to the Brillouin sphere, while for degree  $n=10$  method A is closer to C and for  $n = \{20, 100\}$  method B is closer to C.

The differences between methods A and C are getting smaller proportionally as the computation point moves away from the Brillouin sphere. Specifically at the far distance point  $P_{45}$ , 33.5 km from the sphere, the agreement of methods A and C is at the  $1E-4$  level for  $n=5$ ,  $1E-6$  for  $n=10$  and  $1E-11$  for  $n = \{20, 100\}$ . At this point the differences of methods A and B are numerically equal to  $0 \text{ m}^2/\text{s}^2$ .

The next case study is the computation of the gravitational potential with both methods at three fixed points with increasing distance from the center of mass as a function of the expansion degree. At each of the three points the contribution  $V_n$  of each degree  $n = \{0, 1, \dots, 100\}$  was extracted and compared with the constant value of the analytical solution.

Those three points under examination are taken from the previous scenario of the 45 points with increasing distance from the center of mass and are identified with the points numbered 12, 21 and 31. They are positioned in 3D space as shown with green color in Fig. 4 while their polar coordinates are shown in Table 4.

Starting from the nearest point  $P_{12}$ , the gravitational potential computed with methods A and C separated into four smaller view windows for different degree ranges is shown in Fig. 11. The corresponding diagram for point  $P_{21}$  is shown in Fig. 12 and for point  $P_{31}$  in Fig. 13.

The convergence between methods A and C is faster as the distance of the computation point from Eros increases, as expected. At point  $P_{12}$  the two methods agree at the  $1E-5$  level after  $n=50$ , the same level of agreement being reached at point  $P_{21}$  after  $n=14$  and

**Fig. 9** 2D planes perpendicular to the x-axis with the 1st row referring to  $X=-30$  km with respect to the center of mass, 2nd  $X=20$  km, 3rd  $=-10$  km, 4th  $=0$  km, 5th  $=10$  km, 6th  $=20$  km and 7th  $=30$  km. The x-axis of the diagrams refers to the Z coordinate in km while the y-axis to Y coordinate. The first column is representing the computed gravitational potential with method A, the second the differences between method A and B, and the last the differences between method A and C. The black circle represents the corresponding Brillouin sphere

at  $P_{31}$  after  $n=8$ . The agreement decreases significantly for smaller degree ranges reaching the  $1E-2$  level after  $n=8$  at point  $P_{12}$  and after  $n=4$  at points  $P_{21}$  and  $P_{31}$ .

Concerning the differences between methods A and B, they agree to the  $1E-15$  level at point  $P_{31}$  and to  $1E-13$  at point  $P_{21}$ . For point  $P_{31}$  method A is closer to solution C than method B, while for point  $P_{21}$  the opposite is true with method B being closer to C.

About point  $P_{12}$  there is an agreement up to the  $1E-12$  level between methods A and B at degrees  $n = \{0, 1, \dots, 6\}$ , slowly decreasing up to  $1E-8$  at  $n=100$ . This happens because the computation point is very close to the Brillouin sphere, about 400 m, and as the expansion degree increases the convergence decreases. At this point there is no clear indication of which method is closer to solution C as they have alternately larger differences.

As seen from the gravitational potential plots the methods after some degree remain on a fixed value parallel to the constant value of method C. Concerning point  $P_{12}$  neither method A nor B converge to a fixed potential value. For point  $P_{21}$  the constant part begins at degree  $n=49$  for method A and at  $n=53$  for method B, while for point  $P_{31}$  both methods converge to a constant value already by  $n=31$ .

### 3.2 Didymos

Asteroid 65,803 Didymos (Fig. 14) is characterized as a near Earth asteroid and was discovered in April 1996. Its 3D shape model is produced from radar observations which took place in November 2003 (Naidu et al. 2020).

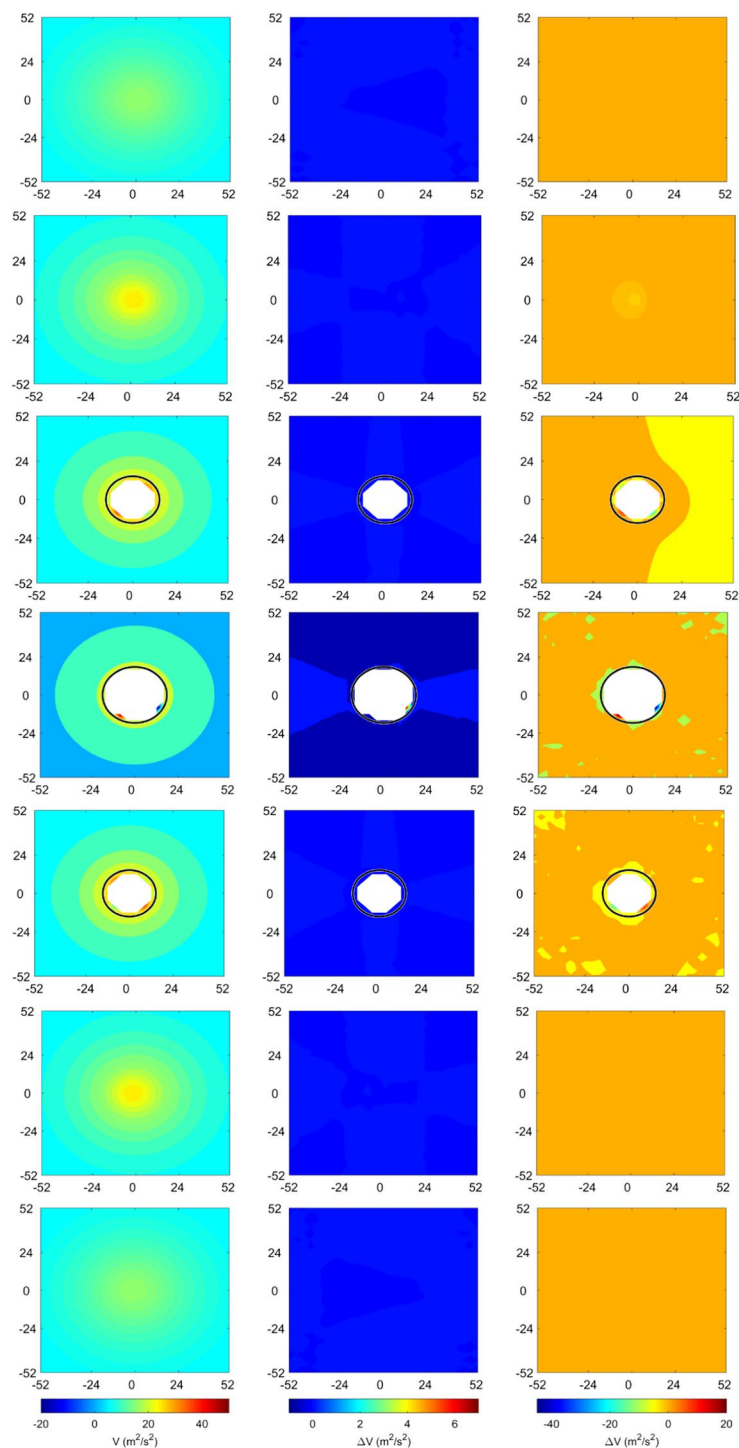
The total calculated volume is  $0.249 \text{ km}^3$  while the density is assumed equal to  $2170 \text{ kg/m}^3$ . The required CPU time for methods A and B with the corresponding radii of the Brillouin, Bjerhammar and mean sphere are shown in Table 1. Due to the almost spherical shape of Didymos, the three spheres are quite similar and the uncertainty region of the results around the surface of the asteroid is smaller (Fig. 14).

The absolute differences between the two methods for the coefficients  $\bar{C}_{nm}$  and  $\bar{S}_{nm}$  are smaller than  $1E-8$ . The range of the differences is larger than 10 in comparison with those of Eros but the rms value is smaller. Specifically, for Didymos the rms is about  $4.5E-11$  while for Eros  $6E-11$ .

The computations for degree and order variances (38), (39) are taking place for both methods A and B. The square root of degree and order variances' rms are both equal to  $9.951E-2$  for method A while method B has a higher rms value by  $1E-16$ . In the case of Eros, the opposite was true with method A having bigger rms value.

The graphical representations of the square root of degree and order variances, their absolute differences and the square root of difference degree and order variances are presented in Fig. 15. The statistical indicators for the square root of degree and order variances' absolute differences (40), (41) between the two methods, as well as for the square root of difference degree and order variances are shown in Table 5.

The absolute differences for the square root of degree variances are ranging from 0 to  $4.4E-10$  with rms  $9.2E-11$  and for the order variances from  $2.2E-16$  to  $1.6E-9$  with rms  $3.7E-10$ . The range in those differences has the same order of magnitude as in Eros



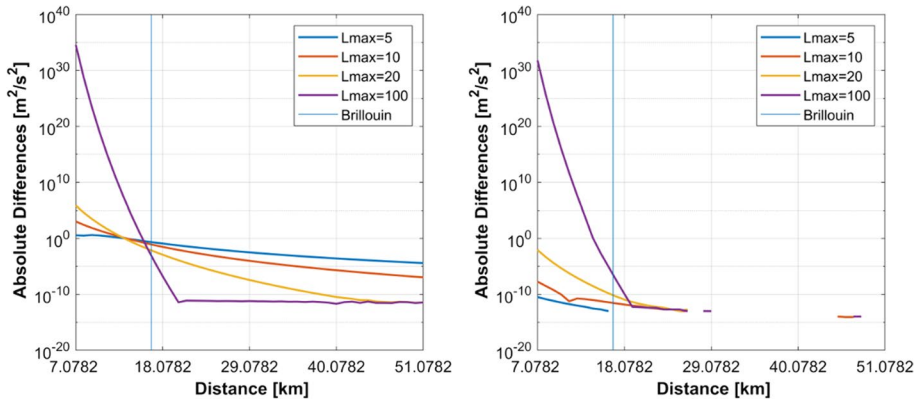


**Fig. 10** (left) Absolute differences in the value of gravitational potential from method A with method C and (right) with method B, in relation with the distance of the computation point from the asteroid each time, at logarithmic scale. The vertical blue line represents the radius  $R_{\max}$  of the Brillouin sphere

(Table 2), while the rms has smaller value. Specifically, the absolute differences of square root degree variances' rms for Didymos is  $9.2\text{E-}11$  and for Eros  $4\text{E-}10$ , while the absolute differences of square root order variances' rms for Didymos is  $3.7\text{E-}10$  and for Eros  $4.1\text{E-}10$ .

The square root of the difference degree variances and difference order variances range between about the same values as in Eros, from 0 to  $1.6\text{E-}9$  and from  $3.7\text{E-}11$  to  $1.7\text{E-}9$ , respectively. Their rms has the same value for both difference degree and order variances and is nearly 25% decreased than in Eros, specifically  $6.2\text{E-}10$  for Eros and  $4.5\text{E-}10$  for Didymos. Asteroid Psyche seems to have slightly better statistical behavior than Eros but considering the graphical illustrations in diagrams (5), (15) it appears to have abrupt variations.

The next computed relative statistical indicator is correlation by degree (44) and correlation by order (45) as shown in Fig. 16. The methods A and B have correlation by degree up to 100% until degree 49 and correlation by order up to 100% until order 31, while for Eros they were in complete agreement until degree 45 and order 42, respectively. From there on, the correlation by degree and order decreases to 99.996% and 99.696%, respectively. The smoothing per degree (46) and smoothing per order (47) are shown in Fig. 17. The smoothing per degree ranges from  $3\text{E-}24$  to  $1.6\text{E-}4$  and per order from  $5\text{E-}21$  to  $2\text{E-}2$ , specifically 3 orders of magnitude bigger than Eros.

The two gravity models from methods A and B, for the case of Didymos, are more different as inferred from the values of correlation and smoothing than in the case of Eros, but as seen from the variances the internal accuracy of each model separately for Didymos is better, probably due to its almost spherical shape.

For the evaluation of the effectiveness of the extracted coefficients to spherical harmonic synthesis we followed the same path as for Eros. The first scenario took in account the computation of the gravitational potential at 4375 arbitrary points in the 3D space around the mass distribution, normally distributed and creating a 3D grid. A total of 7 planes were considered (Fig. 18), with every one consisting of 25 points at the  $z$ - and  $y$ -axis, from  $-2.4$  to  $2.4$  km with respect to the center of mass, while the  $x$  coordinate remained constant and varying for each plane between  $-1.5$  km and  $1.5$  km. The results are shown in Fig. 19.

**Table 3** Absolute differences of the potential between the three examined methods for the 11 points inside the Brillouin sphere of Eros. The units are  $\text{m}^2/\text{s}^2$

Point	$r_{\text{max}}$	5	10	20	100
1	A-C	3.76777357794080E+00	1.10469879180111E+03	7.27046157966932E+05	3.75804267410576E+34
	A-B	3.31041860590631E-11	1.91901108337333E-08	8.87557899113745E-03	6.36724575873998E+31
	B-C	3.76777357797391E+00	1.10469879178192E+03	7.27046149091353E+05	3.76440991986450E+34
2	A-C	3.23671336060490E+00	2.72353457246954E+02	4.19690867920399E+04	5.73726441749752E+28
	A-B	1.44027012538572E-11	3.40801875609031E-09	5.35456900252029E-04	8.21880795624014E+25
	B-C	3.23671336059050E+00	2.72353457243546E+02	4.19690862565830E+04	5.74548322545376E+28
3	A-C	4.16152603053400E+00	7.94520986612384E+01	3.36860243510909E+03	4.16822542666744E+23
	A-B	6.89936996423057E-12	6.29100327387278E-10	4.43375802205992E-05	4.92572233167001E+20
	B-C	4.16152603052710E+00	7.94520986606093E+01	3.36860239077151E+03	4.17315114899911E+23
4	A-C	3.44205234345400E+00	2.61572232126537E+01	3.52687314781250E+02	1.03967208956039E+19
	A-B	3.39639427693328E-12	9.42002031933953E-11	4.70301000632389E-06	9.78509797029888E+15
	B-C	3.44205234345061E+00	2.61572232125595E+01	3.52687310078240E+02	1.04065059935742E+19
5	A-C	2.47613972004530E+00	9.39900310540350E+00	4.59888576766907E+01	7.04850677679009E+14
	A-B	1.80477854883065E-12	5.80158143748122E-12	6.07934410368216E-07	5.00594040108000E+11
	B-C	2.47613972004350E+00	9.39900310540930E+00	4.59888570687563E+01	7.05351271719117E+14
6	A-C	1.66835987813440E+00	3.60859696833261E+00	7.1966885307260E+00	1.09262379436007E+11
	A-B	1.00186525742174E-12	1.80975234798098E-11	9.22479017617661E-08	5.33513174270020E+07
	B-C	1.66835987813339E+00	3.60859696835070E+00	7.19668844082469E+00	1.09315730753434E+11
7	A-C	1.08739306827420E+00	1.46274671448650E+00	1.30981535092540E+00	3.39534858945180E+07
	A-B	6.03961325596085E-13	1.44027012538572E-11	1.59673945177019E-08	9.33300793100148E+03
	B-C	1.08739306827360E+00	1.46274671450090E+00	1.30981533495800E+00	3.39627389024490E+07
8	A-C	6.98479408931895E-01	6.22297640052999E-01	2.70207880269901E-01	1.90918582789181E+04
	A-B	2.98427949019242E-13	9.70601377048297E-12	3.08550340832880E-09	1.32714525180199E+00
	B-C	6.98479408931597E-01	6.22297640062705E-01	2.70207877184397E-01	1.90931854241699E+04

**Table 3** (continued)

Point	$n_{\max}$	5	10	20	100
9	A-C	4.47593069735802E-01	2.77039987951000E-01	6.19376333176014E-02	1.79079959875729E+01
	A-B	2.02504679691629E-13	6.10000938650046E-12	6.56200427329168E-10	2.29648198529908E-03
	B-C	4.47593069735600E-01	2.77039987957100E-01	6.19376326614010E-02	1.79056995055876E+01
	A-C	2.88465637575001E-01	1.28787795034100E-01	1.55425308555017E-02	2.62404616386007E-02
10	A-B	9.94759830064140E-14	3.79785092263774E-12	1.53001167291222E-10	8.36488780109335E-06
	B-C	2.88465637574902E-01	1.28787795037898E-01	1.55425307025006E-02	2.62320967507996E-02
	A-C	1.87928373770298E-01	6.23725128101995E-02	4.22198306659993E-03	5.69216153998298E-05
	A-B	0.00000000000000E+00	2.40163444686914E-12	3.96020993775892E-11	2.86048980058240E-08
11	B-C	1.87928373770298E-01	6.23725128126011E-02	4.22198302699783E-03	5.68930105018239E-05

**Table 4** Polar coordinates of the three independent points for asteroid Eros with respect to the minimum and maximum radius of the corresponding Bjerhammar and Brillouin sphere

	$r$ (m)	$\theta$ (deg)	$\lambda$ (deg)
Bjerhammar	3218.9	—	—
Brillouin	17648.1	—	—
$P_{12}$	18078.2	68.26	− 47.7
$P_{21}$	27078.2	68.26	− 47.7
$P_{31}$	37078.2	68.26	− 47.7

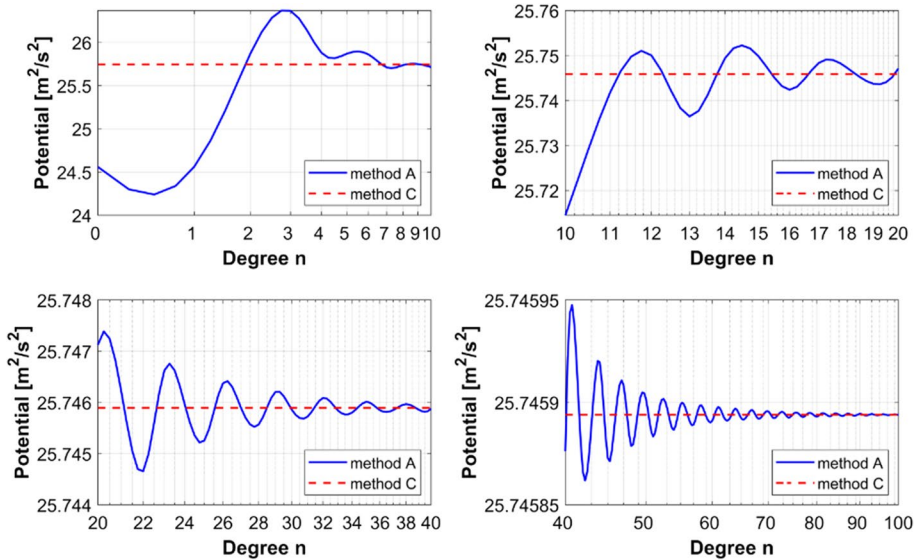


**Fig. 11** Contribution per degree of the gravitational potential at the point P12 with methods A and C on a semilog scale

The definition of these planes in relation to the asteroid, has been chosen so that the distance of the furthest plane from the center of mass to be approximately 3 times the mean radius of the attracting body.

For the comparison of the three methods, at the areas near the edges of the 2D grid at each plane, the differences between methods A and B are about  $1E-18$ , while for Eros the differences were at the  $1E-15$  level. Between methods A and C, the differences are about  $1E-7$  at planes 1–3 and  $1E-15$  at planes 4–7, while for Eros they were  $1E-3$  and  $1E-12$ , respectively. The comparisons are of the differences in gravitational potential values between the methods for each asteroid separately, so there is no question of scale factors  $GM/a$ . Thus, for Didymos it can be deduced that the agreement between the methods increases to about three orders of magnitude compared to the Eros case.

For the second scenario, the gravitational potential for  $k = \{1, 2, \dots, 45\}$  computation points (Fig. 14) was computed using methods A and B. All points  $P_k$  have the same value for  $\theta_k$  and  $\lambda_k$  as shown in Table 7, while the distance  $r$  is given by:  $r_k = 408.5m + (k - 1) * 50m$ .

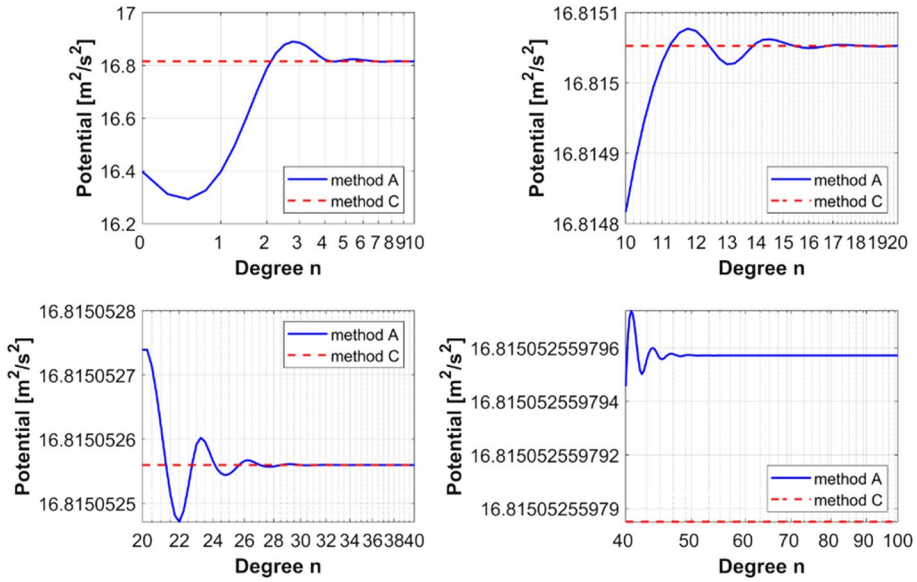


**Fig. 12** Contribution per degree of the gravitational potential at the point P21 with methods A and C on a semilogx scale

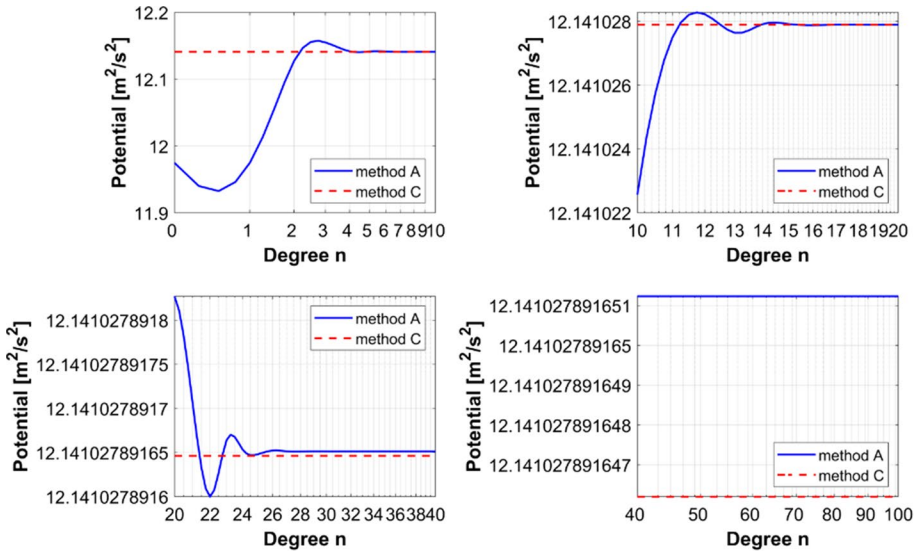


**Fig. 13** Contribution per degree of the gravitational potential at the point P31 with methods A and C on a semilogx scale

The gravitational potential was computed at each point  $P_k$  for varying degree  $n = \{5, 10, 20, 100\}$ , with both spherical approaches compared with the results of the closed analytical value of method C.



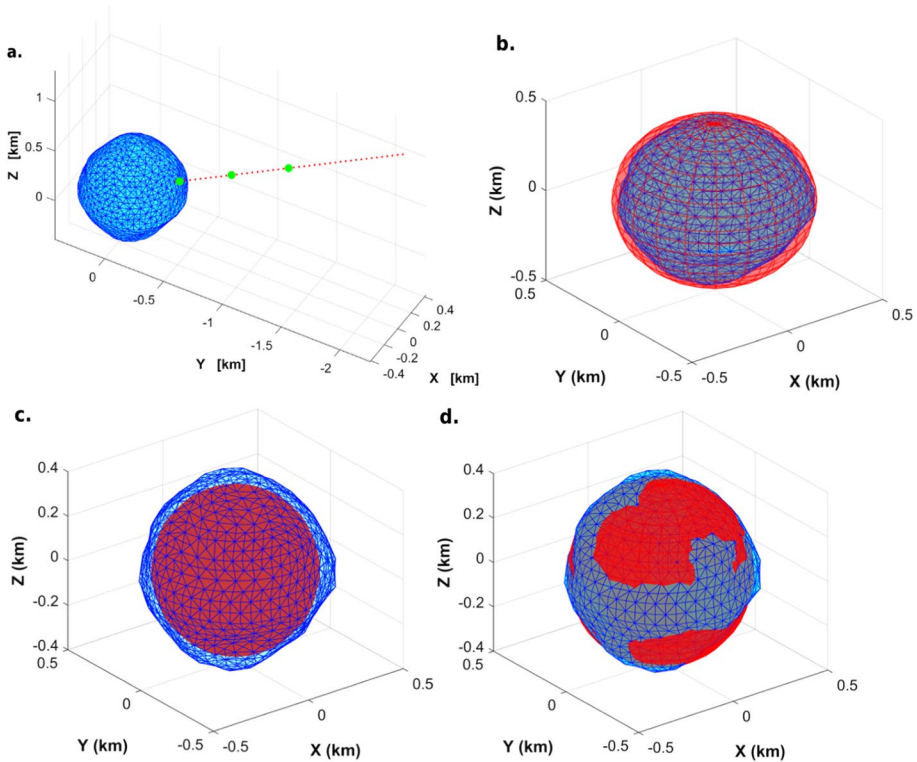


**Fig. 14** Asteroid Didymos in blue color and (b) Brillouin sphere, (c) Bjerhammar sphere and (d) mean radius sphere in red color. Also, (a) the 45 computation points (red dots) with the three selected (green dot) and their position in the 3D space with respect to the asteroid

**Table 5** Statistical indicators for the absolute differences of the square root degree variances, absolute differences of the square root order variances, square root of difference degree variances and square root of difference order variances derived from methods A and B for asteroid Didymos

	$[D_n]$	$[D_m]$	$[\Delta\sigma_n]$	$[\Delta\sigma_m]$
Min	0	2.2204E-16	0	3.7481E-11
Max	4.3779E-10	1.6035E-09	1.6129E-09	1.7441E-09
Mean	4.7052E-11	1.7759E-10	2.6620E-10	2.8922E-10
Rms	9.1786E-11	3.7519E-10	4.5554E-10	4.5554E-10

In the first diagram of Fig. 20 the differences between methods A and C are given in a logarithmic scale, while the second diagram presents the differences between methods A and B.

This time only  $P_1$  lays inside the Brillouin sphere for about 20 m, while  $P_2$  is about 20 m away from this boundary. The absolute differences of the computed gravitational potential between the three models for those 2 points are shown at Table 6. Between methods A and C, for  $P_1$  there is an agreement at the  $1E-5$  level for  $n=100$ ,  $1E-4$  for  $n=\{10, 20\}$  and  $1E-3$  for  $n=5$ . At the  $P_2$  outside the sphere there is an agreement at the  $1E-11$  level for

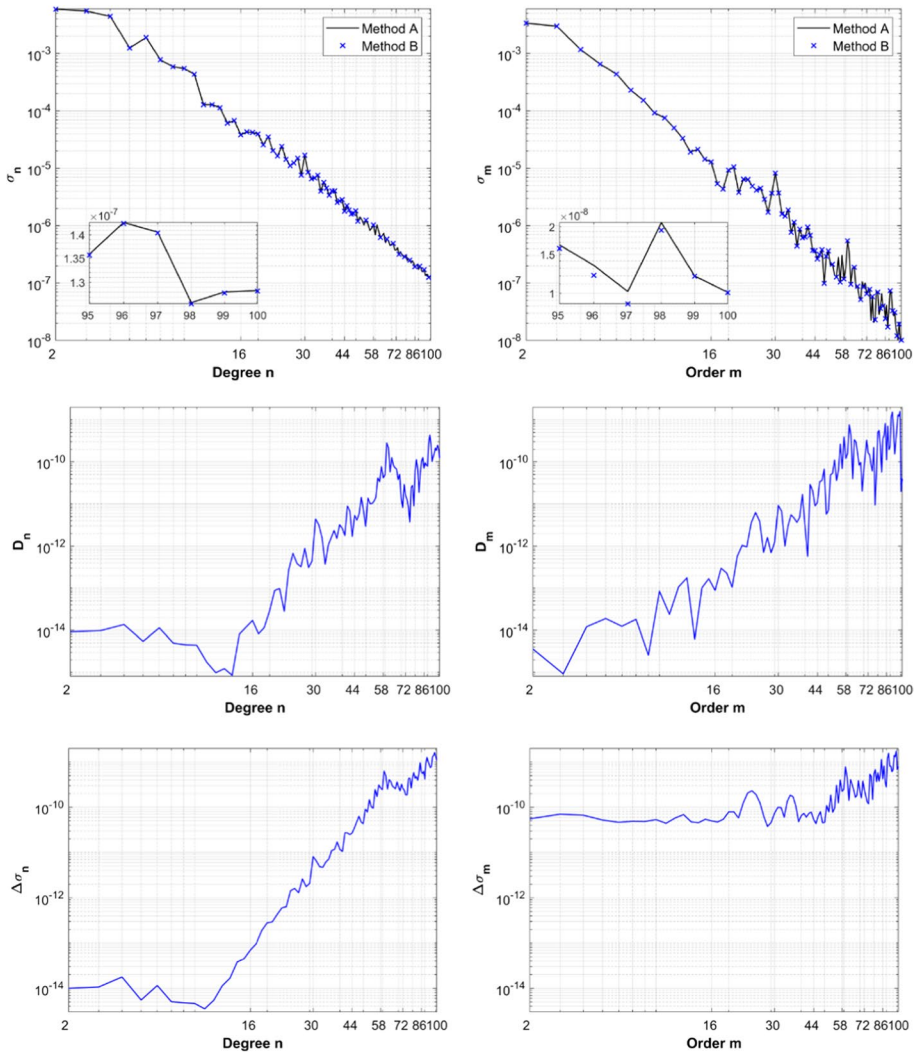


**Fig. 15** Potential coefficient spectra of the two examined methodologies for asteroid Didymos, in logarithmic scale. Upper panel: square root of degree (left) and order (right) variances. Middle panel: absolute differences of square root degree and order variances. Lower panel: square root of difference degree and order variances

$n = 100$ ,  $1\text{E-}5$  for  $n = \{10, 20\}$  and  $1\text{E-}4$  for  $n = 5$ . From there on, the differences are getting smaller reaching an agreement at the  $1\text{E-}9$  level at the point  $P_{45}$  for  $n = 5$  and  $1\text{E-}14$  for  $n = \{10, 20, 100\}$ .

About the differences between the two spherical harmonic methods A and B, there are only some differences at the points close to the body, while as the computation point moves away the differences numerically equal to  $0 \text{ m}^2/\text{s}^2$ . Specifically, the two methods agree at the  $1\text{E-}14$  level for points  $P_1$  and  $P_2$  at  $n = \{5, 10, 20\}$ , the agreement reduces to the  $1\text{E-}8$  level for  $P_1$  and to  $1\text{E-}12$  for  $P_2$  at  $n = 100$ . At point  $P_1$  inside the Brillouin sphere, method

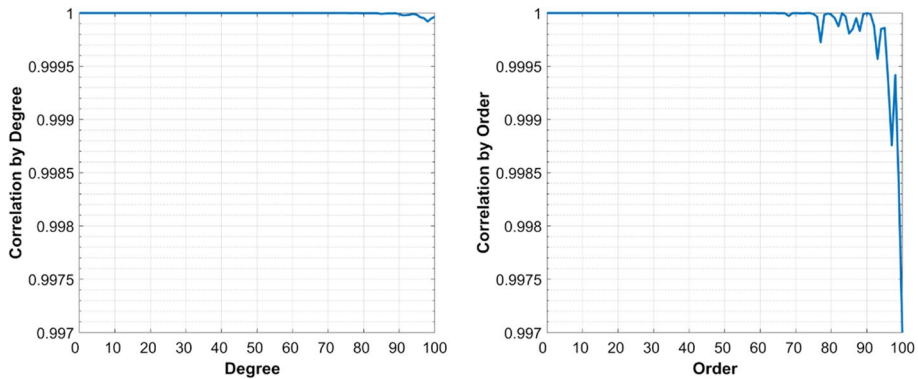


**Fig. 16** (left) Correlation by degree and (right) correlation by order in logarithmic scale between the two sets of fully normalized spherical harmonic coefficients

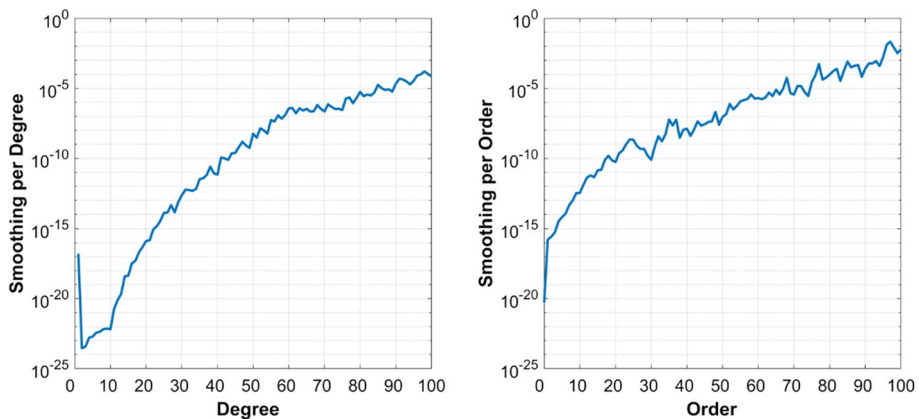


**Fig. 17** (left) Smoothing per degree and (right) smoothing per order in logarithmic scale

A is closer to C thus having smaller differences for degree  $n = \{5, 10, 100\}$ , while at point  $P_2$  only at  $n = \{5, 10\}$ . For the rest of the points, method A is closer to C with an exception at  $n=5$  and at  $n=100$  for  $P_3, P_4$ , where the opposite is true with method B being closer to C.

The last examined scenario is the gravitational potential which derives from methods A and B at three fixed points with increasing expansion degree. The position in 3D space of the three points is shown with green color in Fig. 14. The points are selected from the previous 45 points, more specifically they are identified with points numbered 2, 12 and 23. Their exact polar coordinates are shown in Table 7.

Starting from point  $P_2$ , the gravitational potential derived by method A compared to the constant value of method C separated again into four smaller view windows with different degree ranges is shown in Figs. 21, 22 and 23 are showing the corresponding diagrams for points  $P_{12}$  and  $P_{23}$ , respectively.

Comparing methods A and C, they agree for point  $P_{12}$  at the  $1E-5$  level after degree  $n=3$  and for point  $P_{23}$  already after  $n=1$ . For  $n=100$ , the agreement increases at the  $1E-13$

**Fig. 19** 2D planes perpendicular to the  $x$ -axis with the 1st row referring to  $X = -1.5$  km with respect to the center of mass, 2nd  $X = -1$  km, 3rd  $= -0.5$  km, 4th  $= 0$  km, 5th  $= 0.5$  km, 6th  $= 1$  km and 7th  $= 1.5$  km. The  $x$  axis of the diagrams refers to the  $Z$  coordinate in km while the  $y$  axis to  $Y$  coordinate. The first column is representing the computed gravitational potential with method A, the second the differences between method A and B, and the last the differences between method A and C. The black circle represents the corresponding Brillouin sphere

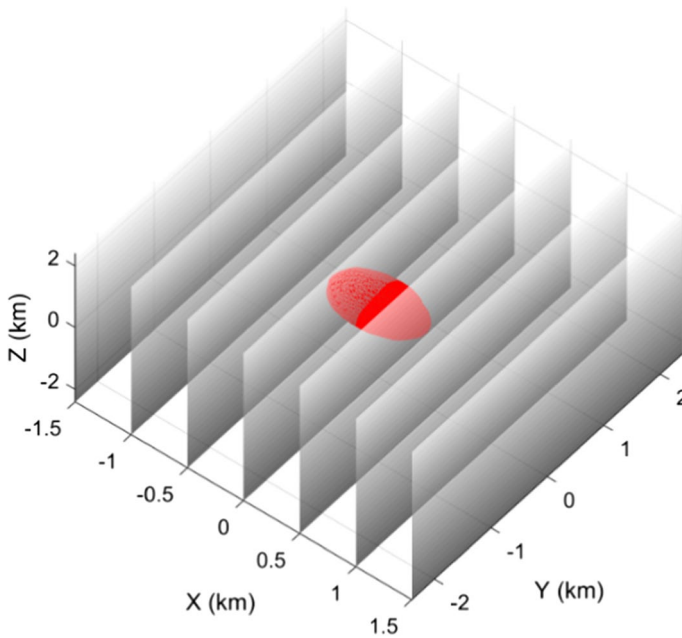
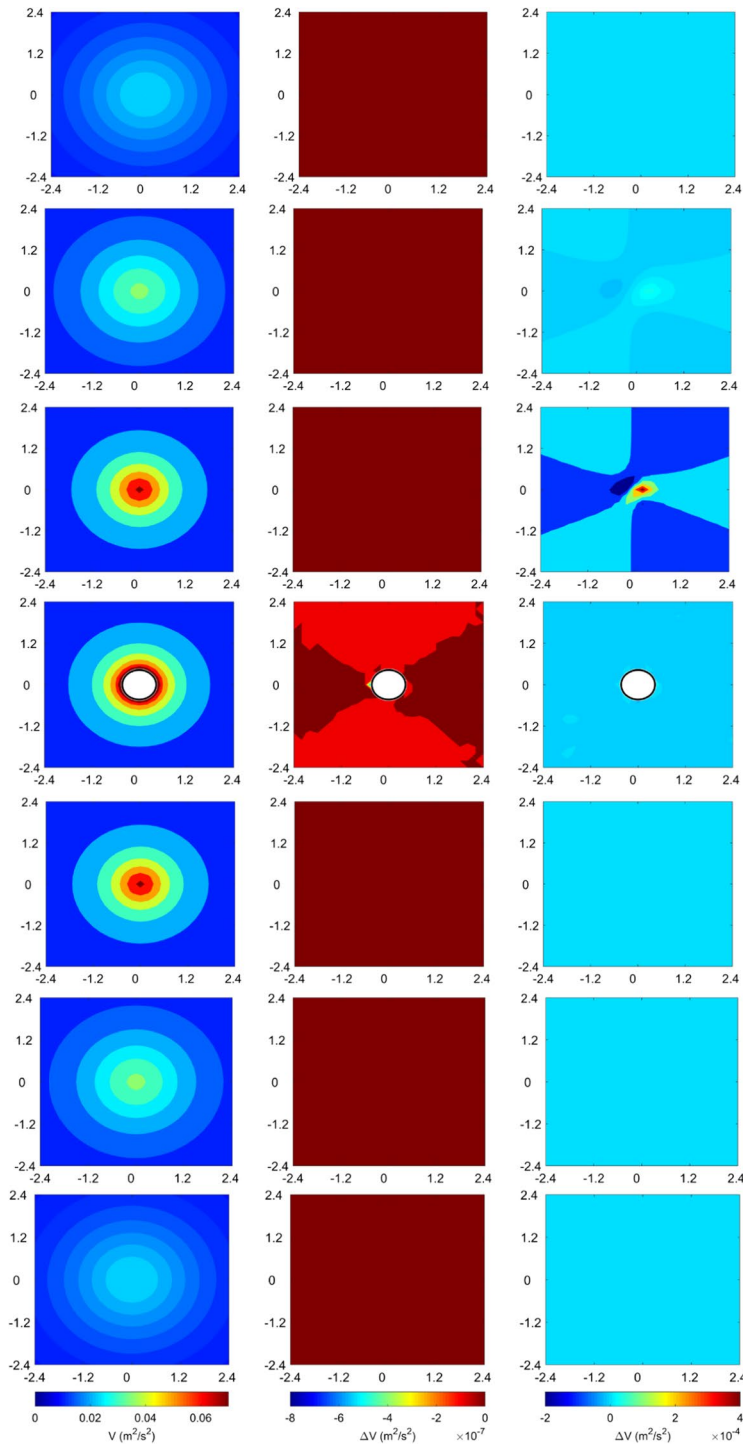


**Fig. 18** 2D planes for the computation of gravitational potential with respect to the asteroid Didymos

level for both points  $P_{12}$  and  $P_{23}$ . Concerning point  $P_2$ , the closest one to the Brillouin sphere, the diagram in Fig. 21 present abrupt variations while methods A and C agree at the  $1E-5$  level after  $n=10$  and at the  $1E-11$  level at  $n=100$ .

For the comparison of methods A and B, the results for point  $P_{23}$  are identical while for point  $P_{12}$  they agree at the  $1E-15$  level with method B being closer to the solution of method C. For point  $P_2$  the agreement starts at  $n=1$  at the  $1E-15$  level until  $1E-12$  at  $n=100$ , while method A is closer to the analytical solution after  $n=15$ .

Regarding the convergence of the potential value with respect to the analytical solution, at point  $P_2$  neither of the methods converges to a fixed value, at point  $P_{12}$  method A converges to a constant value after degree  $n=29$  and method B does the same after  $n=32$ , while at point  $P_{23}$  both methods remain to a constant potential value after  $n=19$ .



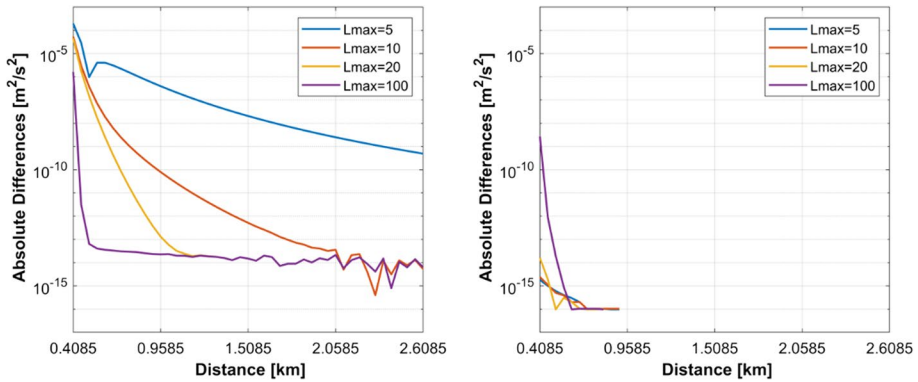


**Fig. 20** (left) Absolute differences in the value of gravitational potential from method A with method C and (right) with method B, in relation with the distance of the computation point from the asteroid each time, at logarithmic scale. The line representing the boundary of the Brillouin sphere is not seen, as it includes only one point and is very close to the y-axis

**Table 6** Absolute differences of the potential between the three examined methods for 2 points near the Brillouin sphere of Didymos. The units are  $m^2/s^2$ .

Point	$n_{\max}$	5	10	20	100
1	A–C	1.93940827883099E-04	5.38504356874942E-05	4.52551352806974E-05	1.62800700739818E-06
	A–B	1.80411241501588E-15	2.40085729075190E-15	1.59039448277554E-14	2.68206659659320E-09
	B–C	1.93940827884903E-04	5.38504356898950E-05	4.52551352647934E-05	1.63068907399477E-06
2	A–C	2.88758346079915E-05	2.97303066429389E-06	1.75319693009046E-06	3.14639980736331E-12
	A–B	9.99200722162641E-16	1.09634523681734E-15	1.90125692967058E-15	8.80906458888831E-13
	B–C	2.88758346089907E-05	2.97303066539023E-06	1.75319692818920E-06	2.26549334847448E-12

**Table 7** Polar coordinates of the three independent points for the asteroid Didymos with respect to the minimum and maximum radius of the corresponding Bjerhammar and Brillouin sphere

	$r$ (m)	$\theta$ (deg)	$\lambda$ (deg)
Bjerhammar	352.3	–	–
Brillouin	427.5	–	–
$P_2$	458.5	59.991	–88.0681
$P_{12}$	958.5	59.991	–88.0681
$P_{23}$	1508.5	59.991	–88.0681

## 4 Conclusions

The line integral approach for the computation of the spherical harmonic coefficients of a homogeneous polyhedral body is tested on two real three-dimensional mass distributions. It is implemented for the gravitational potential calculation of two asteroids, Eros and Didymos, at the same time being compared with Werner's alternative for the

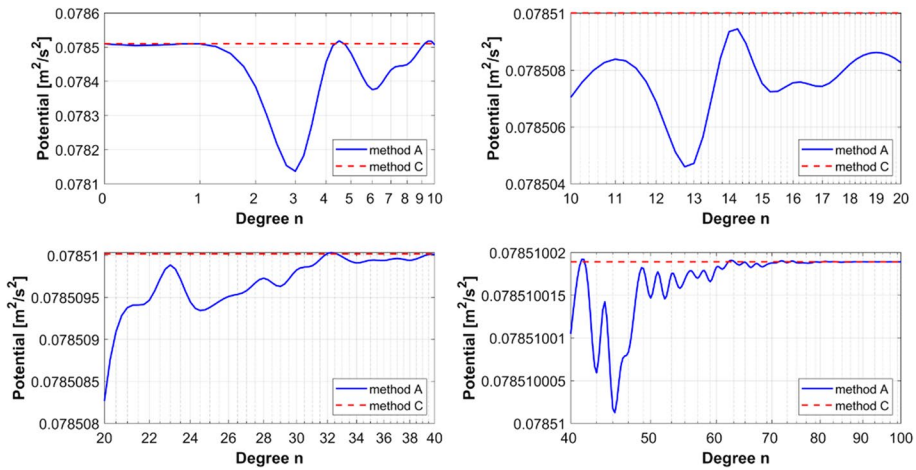


**Fig. 21** Contribution per degree of the gravitational potential at the point P2 with methods A and C on a semilog scale

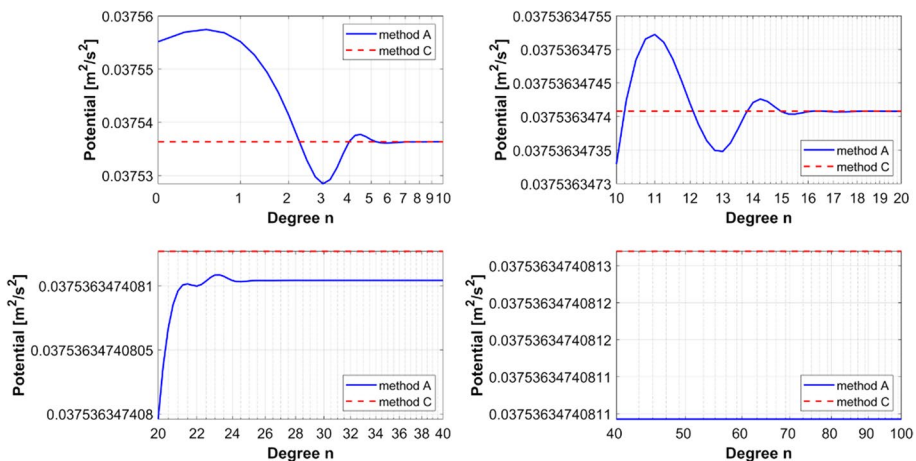


**Fig. 22** Contribution per degree of the gravitational potential at the point P12 with methods A and C on a semilog scale

polyhedral spherical harmonic coefficients and the analytical solution of the generally shaped polyhedron.

The programming computing platform of MATLAB has been used for the implementation of Werner's approach and the analytical methodology, while the line integral approach was evaluated in the Jupyter Notebook environment. From a statistical point of view, the rms of the absolute differences of the computed spherical harmonic coefficients is about  $6\text{E-}11$  for Eros and  $4.5\text{E-}11$  for Didymos. Thus, there is a 25% decrease in the value of the coefficient's absolute differences for the case of Didymos, obviously linked to its spherical shape. The rms of the square root variances' absolute differences is about  $4\text{E-}10$  for Eros while for Didymos it becomes  $1\text{E-}10$  for the degree variances and  $4\text{E-}10$  for the order



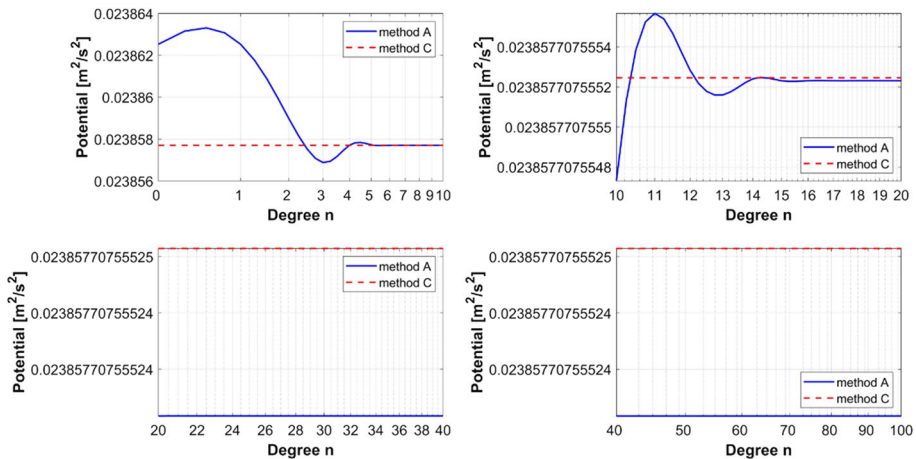


**Fig. 23** Contribution per degree of the gravitational potential at the point P23 with methods A and C on a semilogx scale

variances. Concerning the square root of degree and order variances separately for each method, for Eros the line integral approach has a higher rms value of  $1.5\text{E-}15$ , while for Didymos the opposite is true with Werner's approach having the higher value of  $1\text{E-}16$ . The rms of the square root of difference degree variance has the same value as the rms of the square root of difference order variance for both asteroids' cases, with Eros having about a 25% increased rms value,  $6\text{E-}10$  for Eros and  $4.5\text{E-}10$  for Didymos. The correlation by degree for Eros at degree 100 is 99.9996% and the correlation by order 99.9998%, while for Didymos the corresponding values are 99.996% and 99.696%. In other words, the two methods are correlated slightly less for Didymos than for Eros, about 0.004% for the degree and 0.3% for the order correlation.

Inside the Brillouin sphere and approaching its boundary for the case of Eros there is an agreement in the numerical value of the gravitational potential from the line integral approach and the analytical solution at the  $1\text{E-}4$  level for expansion degree 100, with Werner's approach succeeding a  $1\text{E-}7$  agreement. For Didymos the corresponding agreement levels are  $1\text{E-}5$  and  $1\text{E-}8$ . For both asteroids, the line integral approach seems to overall secure a closer agreement to the analytical solution than Werner's approach. At the furthest examined points, 33.5 km outside the Brillouin sphere for Eros and 2.2 km for Didymos, there is an agreement between the line integral approach and the analytical solution at the  $1\text{E-}11$  level for Eros and at the  $1\text{E-}14$  level for Didymos, while the differences with Werner's approach equal to zero.

From the examination of the gravitational potential deriving from the three methodologies at some independent fixed points, it has been concluded that the line integral approach converges to a fixed numerical value sooner than Werner's approach by a range of 4 degrees.

**Acknowledgements** The first author (GG) was supported by the Hellenic Foundation for Research and Innovation (HFRI) under the 4th Call for HFRI PhD Fellowships (Fellowship Number: 10834). Special thanks to Robert Werner and Olivier Jamet for providing relevant source code. Finally, we would like to acknowledge the detailed comments of two anonymous reviewers, that helped us improve the clarity of the presentation.



## Declarations

**Conflict of Interest** The authors declare no conflict of interest for the present contribution.

## References

- Balmino G (1994) Gravitational potential harmonics from the shape of an homogeneous body. *Celest Mech Dyn Astron* 60:331–364. <https://doi.org/10.1007/BF00691901>
- Chao BF, Rubincam DP (1989) The gravitational field of Phobos. *Geophys Res Lett* 16:859–862. <https://doi.org/10.1029/GL016i008p00859>
- Chen C, Chen Y, Bian S (2019) Evaluation of the spherical harmonic coefficients for the external potential of a polyhedral body with linearly varying density. *Celest Mech Dyn Astron* 131:8. <https://doi.org/10.1007/s10569-019-9885-5>
- Colombo OL (1981) Numerical methods for harmonic analysis on the sphere
- Cunningham LE (1970) On the computation of the spherical harmonic terms needed during the numerical integration of the orbital motion of an artificial satellite. *Celest Mech* 2:207–216. <https://doi.org/10.1007/BF01229495>
- D'Urso MG (2014a) Analytical computation of gravity effects for polyhedral bodies. *J Geodesy* 88:13–29. <https://doi.org/10.1007/s00190-013-0664-x>
- D'Urso MG (2014b) Gravity effects of polyhedral bodies with linearly varying density. *Celest Mech Dyn Astron* 120:349–372. <https://doi.org/10.1007/s10569-014-9578-z>
- D'Urso MG (2015) A remark on the computation of the gravitational potential of masses with linearly varying density. *Int Assoc Geodesy Symposia* 142:205–212. [https://doi.org/10.1007/1345\\_2015\\_138](https://doi.org/10.1007/1345_2015_138)
- Gottlieb RG (1993) Fast gravity, gravitypartials, normalized gravity, gravity gradient torque and magnetic field:derivation, code and data. In: NASA contractor report 188243, Nationalaeronautics and space administration lyndon B. Johnson Space Center Houston,TX, United States
- Heiskanen WA, Moritz H (1967) Physical geodesy. W. H. Freeman and Company, San Francisco
- Hu X, Jekeli C (2015) A numerical comparison of spherical, spheroidal and ellipsoidal harmonic gravitational field models for small non-spherical bodies: examples for the martian moons. *J Geodesy* 89:159–177. <https://doi.org/10.1007/s00190-014-0769-x>
- Jamet O, Tsoulis D (2020) A line integral approach for the computation of the potential harmonic coefficients of a constant density polyhedron. *J Geodesy* 94:30. <https://doi.org/10.1007/s00190-020-01358-8>
- Jamet O, Thomas E (2004) A linear algorithm for computing the spherical harmonic coefficients of the gravitational potential from a constant density polyhedron. In: Proceedings of the 2nd international GOCE user workshop “GOCE, the geoid and oceanography”, ESA-ESRIN, Frascati, Italy, 8–10 March 2004, ESA SP-569, June 2004
- Lien SL, Kajiya JT (1984) A symbolic method for calculating the integral properties of arbitrary non-convex polyhedra. *IEEE Comput Graph Appl* 4:35–42. <https://doi.org/10.1109/MCG.1984.6429334>
- Miller JK, Konopliv AS, Antreasian PG, Bordi JJ, Chesley S, Helfrich CE, Owen WM, Wang TC, Williams BG, Yeomans DK, Scheeres DJ (2002) Determination of shape, gravity, and Rotational State of Asteroid 433 Eros. *Icarus* 155:3–17. <https://doi.org/10.1006/icar.2001.6753>
- Nagy D, Papp G, Benedek J (2000) The gravitational potential and its derivatives for the prism. *J Geodesy* 74:552–560. <https://doi.org/10.1007/s001900000116>
- Naidu SP, Benner LAM, Brozovic M, Nolan MC, Ostro SJ, Margot JL, Giorgini JD, Hirabayashi T, Scheeres DJ, Pravec P, Scheirich P, Magri C, Jao JS (2020) Radar observations and a physical model of binary near-Earth asteroid 65803 Didymos, target of the DART mission. *Icarus* 348:113777. <https://doi.org/10.1016/j.icarus.2020.113777>
- Petrović S (1996) Determination of the potential of homogeneous polyhedral bodies using line integrals. *J Geodesy* 71:44–52. <https://doi.org/10.1007/s001900050074>
- Rummel R, Rapp RH, Suenkel H, Tscherning CC (1988) Comparisons of global topographic/isostatic models to the Earth's observed gravity field
- Saraswati AT, Cattin R, Mazzotti S, Cadio C (2019) New analytical solution and associated software for computing full-tensor gravitational field due to irregularly shaped bodies. *J Geodesy* 93:2481–2497. <https://doi.org/10.1007/s00190-019-01309-y>

- Singh B, Guptasarma D (2001) New method for fast computation of gravity and magnetic anomalies from arbitrary polyhedra. *Geophysics* 66:521–526. <https://doi.org/10.1190/1.1444942>
- Takahashi Y, Scheeres DJ (2014) Morphology driven density distribution estimation for small bodies. *Icarus* 233:179–193. <https://doi.org/10.1016/j.icarus.2014.02.004>
- Tsoulis D (2000) A note on the gravitational field of the right rectangular prism. *Bollettino di Geodesia e Scienze Affini* 59:21–35
- Tsoulis D (2012) Analytical computation of the full gravity tensor of a homogeneous arbitrarily shaped polyhedral source using line integrals. *Geophysics* 77:F1–F11. <https://doi.org/10.1190/geo2010-0334.1>
- Tsoulis D, Gavrilidou G (2021) A computational review of the line integral analytical formulation of the polyhedral gravity signal. *Geophys Prospect* 69:1745–1760. <https://doi.org/10.1111/1365-2478.13134>
- Tsoulis D, Jamet O, Verdun J, Gonindard N (2009) Recursive algorithms for the computation of the potential harmonic coefficients of a constant density polyhedron. *J Geodesy* 83:925–942. <https://doi.org/10.1007/s00190-009-0310-9>
- Tsoulis D, Patlakis K (2013) A spectral assessment review of current satellite-only and combined Earth gravity models. *Rev Geophys* 51:186–243. <https://doi.org/10.1002/rog.20012>
- Tsoulis D, Petrović S (2001) On the singularities of the gravity field of a homogeneous polyhedral body. *Geophysics* 66:535–539. <https://doi.org/10.1190/1.1444944>
- Werner RA (1994) The gravitational potential of a homogeneous polyhedron or don't cut corners. *Celest Mech Dyn Astron* 59:253–278. <https://doi.org/10.1007/BF00692875>
- Werner RA (1997) Spherical harmonic coefficients for the potential of a constant-density polyhedron. *Comput Geosci* 23:1071–1077. [https://doi.org/10.1016/S0098-3004\(97\)00110-6](https://doi.org/10.1016/S0098-3004(97)00110-6)
- Werner RA, Scheeres DJ (1997) Exterior gravitation of a polyhedron derived and compared with harmonic and mascon gravitation representations of asteroid 4769 Castalia. *Celest Mech Dyn Astron* 65:313–344. <https://doi.org/10.1007/BF00053511>

**Publisher's Note** Springer Nature remains neutral with regard to jurisdictional claims in published maps and institutional affiliations.

Springer Nature or its licensor (e.g. a society or other partner) holds exclusive rights to this article under a publishing agreement with the author(s) or other rightsholder(s); author self-archiving of the accepted manuscript version of this article is solely governed by the terms of such publishing agreement and applicable law.